Inorganic Chemistry

pubs.acs.org/IC

Article

Spectroscopic and Theoretical Investigation of High-Spin Square-Planar and Trigonal Fe(II) Complexes Supported by Fluorinated Alkoxides

Léa A. Toubiana,[#] Adam Valaydon-Pillay,[#] Jessica K. Elinburg, Jeffrey W. Bacon, Andrew Ozarowski, Linda H. Doerrer,* and Sebastian A. Stoian*

Cite This: *Inorg. Chem.* 2024, 63, 2370−2387

Read Online

ACCESS | Metrics & More | Article Recommendations | SI Supporting Information

ABSTRACT: The electronic structures and spectroscopic behavior of three high-spin Fe^{II} complexes of fluorinated alkoxides were studied: square-planar $\{K(DME)_2\}_2[Fe(pin^F)_2]$ (**S**) and quasi square-planar $\{K(C222)\}_2[Fe(pin^F)_2]$ (**S′**) and trigonal-planar $\{K(18C6)\}[Fe(OC_4F_9)_3]$ (**T**) where pin^F = perfluoropinacolate and OC_4F_9 = *tris*-perfluoro-*t*-butoxide. The zero-field splitting (ZFS) and hyperfine structure parameters of the $S = 2$ ground states were determined using field-dependent ^{57}Fe Mössbauer and high-field and -frequency electron paramagnetic resonance (HFEPR) spectroscopies. The spin Hamiltonian parameters were analyzed with crystal field theory and corroborated by density functional theory (DFT) and *ab initio* complete active space self-consistent field (CASSCF) calculations. Whereas the ZFS tensor of **S** has a small rhombicity, $E/D = 0.082$, and a positive $D = 15.17\ cm^{-1}$, **T** exhibits a negative $D = -9.16\ cm^{-1}$ and a large rhombicity, $E/D = 0.246$. Computational investigation of the structural factors suggests that the ground-state electronic configuration and geometry of **T**'s Fe site are determined by the interaction of $[Fe(OC_4F_9)_3]^-$ with $\{K(18C6)\}^+$. In contrast, two distinct countercations of **S**/**S′** have a negligible influence on their $[Fe(pin^F)_2]^{2-}$ moieties. Instead, the distortions in **S′** are likely induced by the chelate ring conformation change from $\delta\lambda$, observed for **S**, to the $\delta\delta$ conformation, determined for **S′**.

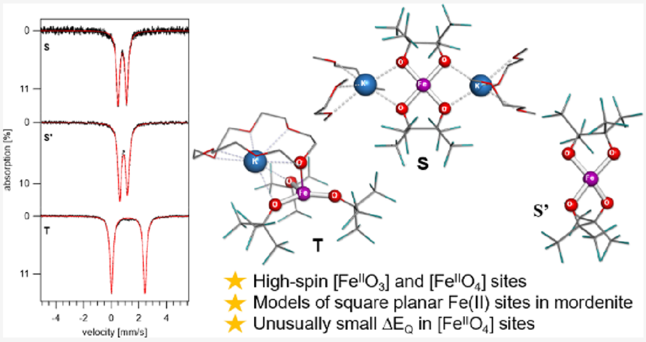

★ High-spin $[Fe^{II}O_3]$ and $[Fe^{II}O_4]$ sites
★ Models of square planar Fe(II) sites in mordenite
★ Unusually small ΔE_Q in $[Fe^{II}O_4]$ sites

1. INTRODUCTION

Oxidation reactions are central to our biology and to technologically important processes including the partial oxidation of methane and water remediation.[1−3] Therefore, oxidation catalysis effected by environmentally benign, high-valent, 3d transition metal-oxo species constitutes a perennial target of bioinorganic research efforts.[4] Metalloenzymes have long been known to perform C−H bond oxidations of various substrates.[5] In particular, Fe-containing enzymes with all N-donor environments have been extensively studied and revealed to use O_2 to form terminal {Fe═O} high-spin intermediates.[6−8] Most importantly, industrial catalysts based on Fe-doped zeolites that enable alkane oxidation with high selectivity and efficiency are also known.[9] Unlike for most enzymes, the active sites of these synthetic species are supported by an all-O-donor environment.

Snyder et al. have used low-temperature MCD[10] and other spectroscopic methods to identify not only the resting state of the Fe-doped zeolites but also their reactive intermediate, the oxidized Fe species that reacts with hydrocarbons. These species incorporate an unusual $[FeO_4]$ site with a square-planar geometry labeled α-Fe(II). When treated with N_2O(g), the α-Fe(II) site of mordenite is converted to an $S = 2$ {Fe(IV)═O} reactive intermediate, which selectively oxidizes methane to methanol. Although there are numerous structural and functional models of enzymatic systems reported to date, there are very few compounds that emulate the active site of Fe-doped zeolites.[11,12]

In this manuscript, we describe the electronic structures of three Fe(II) complexes: the four-coordinate square-planar $\{K(DME)_2\}_2[Fe(pin^F)_2]$ (**S**)[13,14] and quasi square-planar $\{K(C222)\}_2[Fe(pin^F)_2]$ (**S′**) as well as the trigonal-planar $\{K(18C6)\}[Fe(OC_4F_9)_3]$ (**T**)[15] where pin^F = perfluoropinacolate and OC_4F_9 = *tris*-perfluoro-*t*-butoxide. The crystal structures of **S** and **T** as well as of one of the two distinct iron sites per unit cell of **S′** are presented in Figure 1. The first two incorporate an unusual square-planar $[FeO_4]$ structural motif similar to that proposed for the zeolite α-Fe(II) site. Our

Received: September 14, 2023
Revised: December 19, 2023
Accepted: December 22, 2023
Published: January 23, 2024

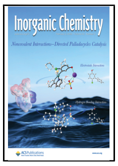

https://doi.org/10.1021/acs.inorgchem.3c03236
Inorg. Chem. 2024, 63, 2370−2387

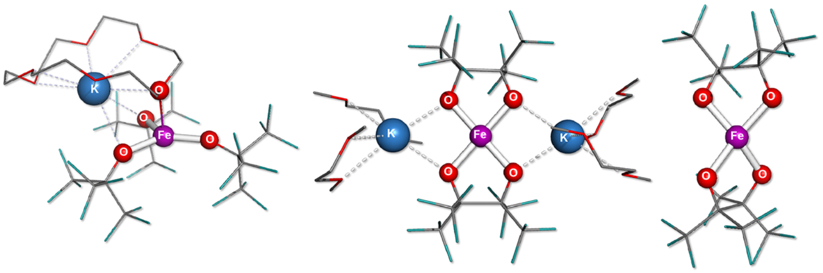

T $\{K(18C6)\}[Fe(OC_4F_9)_3]$

S $\{K(DME)_2\}_2[Fe(pin^F)_2]$

S', *site 1* $\{K(C222)\}_2[Fe(pin^F)_2]$

Figure 1. SCXRD-determined structures of **T**, $\{K(18C6)\}[Fe(OC_4F_9)_3]$ (left), **S**, $\{K(DME)_2\}_2[Fe(pin^F)_2]$ (middle), and *site 1* of **S′**, $\{K(C222)\}_2[Fe(pin^F)_2]$ without cations. Hydrogen atoms were omitted, fluorine atoms shown in teal and carbon atoms in gray. The **S**, **S′**, and **T** labels highlight the square (**S**/**S′**) and trigonal (**T**) geometries of the corresponding iron sites.

Scheme 1. High-Spin Fe(II) Complexes, which Incorporate Iron Sites with an Approximately Square-Planar (Top Row) and Trigonal Planar (Bottom Row) Geometry

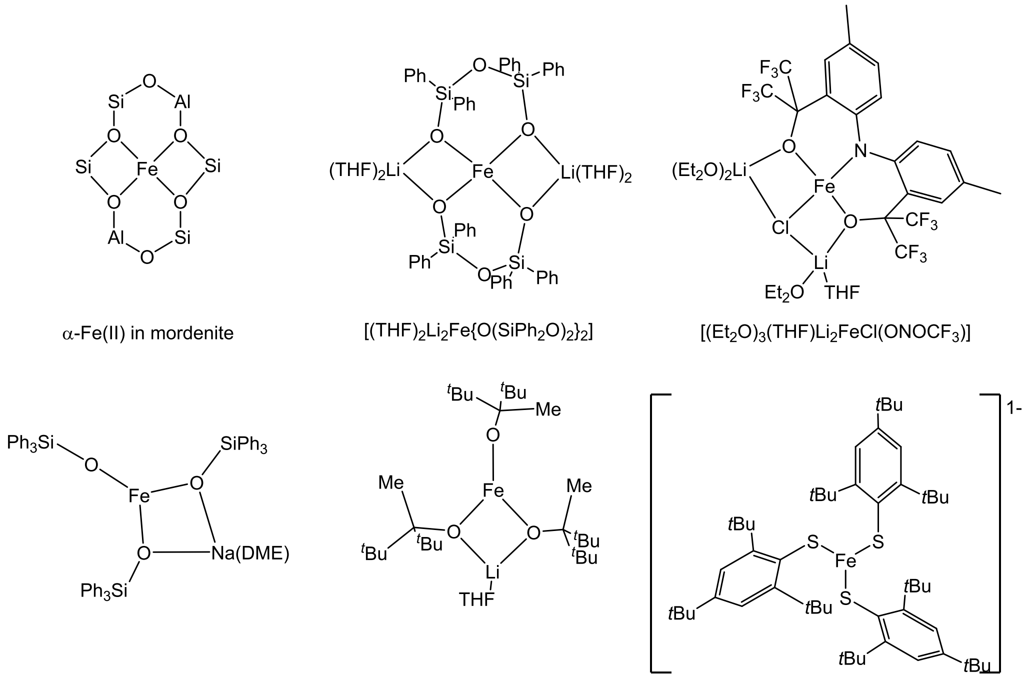

α-Fe(II) in mordenite

$[(THF)_2Li_2Fe\{O(SiPh_2O)_2\}_2]$

$[(Et_2O)_3(THF)Li_2FeCl(ONOCF_3)]$

$[(DME)NaFe(OSiPh_3)_3]$

$[(THF)LiFe(ditox)_3]$

$[Fe\{SC_2(^tBu)_3H_2\}_3]^{1-}$

investigation revealed that **S**/**S′** and α-Fe(II) share many spectroscopic features and have a similar electronic structure. Therefore, this work suggests that **S**/**S′** have the potential to function as good precursors to functional homogeneous catalysis models of Fe-doped zeolites. The electronic structure of the trigonal $\{K(18C6)\}[Fe(OC_4F_9)]$ (**T**) has also been studied. Similar to α-Fe(II), low-coordinate Fe(II) analogues of **T** supported by alkoxo ligands also have the potential to function as precursors for oxidation catalysts. For example, Chambers et al. described an Fe complex with a trigonal tris(alkoxide) ligand environment,[11] $[Fe(OC(tBu)_2(CH_3))_3]^{1-}$, shown in Scheme 1, which reacts with common O-donors Me_3NO and PhIO in THF to yield a proposed reactive intermediate, $[Fe(OC(tBu)_2(CH_3))_3(O)]^{1-}$. This species was supported by DFT calculations and is a rare example of a high-valent {Fe−O} oxidative moiety in an all O-donor environment, capable of abstracting an H atom from MeCN as well as to oxidize PPh_3 to $OPPh_3$. Upon C−H bond cleavage, the intermediate forms an {Fe(III)−OH}-containing species, which was isolated and characterized by X-ray crystallography.[11]

An important structural feature of **S**, **S′**, and **T** is their C−F bonds, which render them much more robust to oxidation than their nonfluorinated analogues, impede intramolecular oxidative degradation, and promote intermolecular substrate C−H bond activation. Moreover, the use of O-donors as ligands results in high-spin complexes,[13−15] increasing the likelihood of high-spin intermediates formed upon reaction with O atom donors, akin to those found in zeolite active sites. The electronic structures of such reactive compounds are largely unexplored. Despite several recent reports of high-spin square planar Fe(II) complexes, compounds such as **S** and **S′** are still extremely rare.[16−20] The few relevant examples of approximately square-planar complexes are shown in the top row of Scheme 1 and include a silicate framework[20,12,21,22] and a tridentate, trianionic ONO pincer ligand.[18,19,23] In most cases, the steric and electronic factors responsible for stabilizing these unusual species are yet to be determined. In this respect, this study fills an important gap in our knowledge and has allowed us to gain new insight into these uncommon sites. While there are only a handful of trigonal, high-spin Fe(II) complexes, such as $Ph_4P[Fe(SR)_3]\cdot 2MeCN\cdot C_7H_8$ where R = C_6H_2-2,4,6-$^tBu_3$,[24] such compounds have played an important role in advancing our understanding of the quasi-trigonal Fe sites of the cofactor of the MoFe protein of nitrogenase enzymes.[25] Moreover, the low coordination number of these species makes them highly reactive and, just as described above, enables them to participate in the activation of small molecules.[26]

2. METHODS AND MATERIALS

2.1. Synthetic Methods. All experimental procedures were carried out on a Schlenk line or in a drybox under an atmosphere of purified N_2 at room temperature. The anhydrous solvents dimethoxyethane (DME), hexanes, toluene, and tetrahydrofuran (THF) were dried in an alumina-based solvent purification system (SPS) under Ar, piped directly into an MBraun drybox, and stored over molecular sieves. Celite was heated to 125 °C under vacuum overnight. KOC_4F_9 was prepared according to a previously published procedure.[15] H_2pin^F was purchased from Oakwood Chemicals and dried over sieves and distilled before use. The ligand salt $KHpin^F$ synthesis was modified from a previous one, by mixing KO^tBu and perfluoropinacol (H_2pin^F) in a 1:1 ratio. All other reagents were obtained commercially and used without any further purification. The compound $\{K(DME)_2\}_2[Fe(pin^F)_2]$ (**S**) was prepared according to a previously published procedure,[13] as was $\{K(18C6)\}[Fe(OC_4F_9)]$ (**T**).[15]

2.2. X-ray Crystallography and Structure Determination. Single-crystal X-ray diffraction of **S′** was collected using a Bruker X8 Proteum-R diffractometer by using CuK_α radiation in a N_2 gas stream at 100(2) K with phi and omega scans. Data were refined using SHELXL 2018/3, and Olex 2 1.5 was used for molecular graphics and preparation of materials for publication.

2.3. Synthesis of S′. In a drybox, $FeCl_2$ (154.7 mg, 1.221 mmol) was stirred in THF (5 mL) for 15 min to give a cloudy off-white suspension. Two equivalents of KN″ where N″ = bis(trimethylsilyl amide) (487.7 mg, 2.441 mmol) were added in THF (3 mL) and left to stir at RT overnight to yield a dark brown cloudy solution. $KHpin^F$ (908.5 mg, 2.441 mmol) was added in THF (3 mL) and left to stir at RT for 2 h to give a dark purple cloudy solution. The solution was filtered through Celite to remove insoluble salts. The purple filtrate was dried *in vacuo* and triturated three times with hexanes. The pale purple powder was extracted into Et_2O and (2,2,2-cryptand) was added (919.0 mg, 2.441 mmol), forming an insoluble blue solid. The Et_2O was concentrated *en vacuo*, and the solid dissolved in THF with drops of DMSO added to increase solubility. The solution was filtered through a pipet, and the best blue crystals were grown by layering the THF/DMSO mixture and toluene at −30 °C in 78% yield (1.47 g). Alternatively, crystals can be grown from a CH_3CN layered with Et_2O, which gave good analytical data but a lower yield. UV−vis(THF) (λ_{max}, nm (ε, $M^{-1}\cdot cm^{-1}$)) 571 (28), 260 (1550). Elemental analysis calculated (%) for $K_2FeC_{48}H_{72}O_{16}F_{24}N_4\cdot MeCN$: C 37.17, H 4.68, F 29.40, N 3.61; found: C 37.01, H 4.88, F 29.35, N 3.62. Evans' method: (CD_2Cl_2) μ_{eff} = 5.20 μ_B.[27]

2.4. ^{57}Fe Mössbauer Spectroscopy. Field and temperature dependent spectra were recorded using a spectrometer operated in a constant acceleration mode. This instrument was equipped with a Janis Varitemp 8DT liquid helium cooled cryostat fitted with an American Magnetics 8 T superconducting coil. Using this spectrometer, data could be acquired at temperatures ranging from 1.7 to 250 K and applied fields of up to 8 T. The applied magnetic field was aligned with the propagation direction of the 14.4 keV γ-ray. The data analysis was performed using the WMOSS (SEE Co. formerly, WEB Research Co., Edina, Minnesota) spectral analysis software as well as C-based Igor Pro codes developed in-house. Isomer shifts are reported against the center of a zero-field spectrum recorded at room temperature for a α-iron metal foil. The Mössbauer absorbers were prepared by dispersing ground neat powders in either a mineral oil such as Nujol or in eicosane. Samples were either shipped under an inert atmosphere in sealed Schlenk flasks or while stored at 77 K using a dry shipping dewar. Upon receipt, the samples were moved to a long-term storage dewar and stored under liquid nitrogen (LN_2). Prior to measurements, the samples were manipulated under LN_2 and loaded in the spectrometer while cold.

2.5. High-Frequency EPR. The HFEPR spectra were acquired using a transmission-type instrument equipped with a 17 T Oxford Instruments superconducting magnet.[28] Desired microwave frequencies were obtained using a 12−14 GHz Virginia Diodes phase-locked source in combination with several frequency multipliers used to produce higher-frequency harmonics. Spectral analysis was performed using the SPIN program and C-based Igor Pro codes developed in-house.[29] All samples were shipped while kept at 77 K using a LN_2 dry shipper. Moreover, the samples were stored under liquid nitrogen transferred to the spectrometers or a glovebox for further grinding and dispersing in Nujol while cold. The HFEPR samples were contained in polyethylene cups fitted with Teflon stoppers and were investigated by zero-field Mössbauer spectroscopy to assess the purity and viability of each sample (Scheme 2).

Scheme 2. Five-Membered Ring with λ and δ Chelate Ring Conformations Experimentally Observed for the $[Fe(pin^F)_2]^{2-}$ Anions

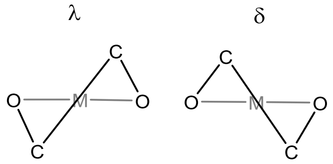

2.6. Computational Methods. Density functional theory (DFT) and complete active space self-consistent field (CASSCF) calculations were performed using the ORCA 5.0 quantum mechanical computation package.[30,31] Benchmark coupled-perturbed (CP) and single-point DFT calculations were performed using the hybrid B3LYP,[32] GGA BP86,[33] and meta-GGA TPSSh[34] functionals in combination with the Pople 6-311G[35] and Ahlrichs triple-ζ def2-TZVPP[36] basis sets. CASSCF calculations were additionally performed using the def2-TZVPP basis set. In order to ease computational burden, the RI-J approximation was used for all calculations, RI-JK was used when employing the BP86 functional, and the RI-JCOSX "chain of spheres" approximation was used with the B3LYP and TPSSh functionals.[37,38] The auxiliary basis sets Aux-C, Aux-J, and Aux-JK were included as necessary with the *autoaux* command.[39] In all cases, calculations were converged slowly to tight convergence criteria by employing the *slowconv* and *tightscf* commands, respectively. In all CP and single-point calculations, convergence to the ground state was verified with subsequent time-dependent (TD) DFT calculations, for which all transitions occurred at positive energies. Geometry optimizations were performed using the full or simplified experimental structures of **T**, **S**, and **S′** as initial inputs in combination with the *opt* ORCA keyword. Structural models of $[Zn(pin^F)_2]^{2-}$ were obtained by replacing the iron(II) ions of the corresponding $[Fe(pin^F)_2]^{2-}$ models with zinc(II) and reoptimizing the resulting structures. CASSCF(5,6) calculations were performed considering six electrons distributed over five orbitals that comprise the canonical 3d orbitals of the Fe(II) ion. Corrections to the obtained CASSCF correlation energies were provided by NEVPT2 methods.[40] The triplet states' contribution to the ZFS were estimated from the difference between the ZFS parameters derived from calculations, which only considered the quintet states and those obtained when both the quintet and the triplet were included in the calculations. Theoretical isomer shifts were calculated at the B3LYP, BP86, TPSSh/TZVP, and B3LYP/6-311G levels of theory using the linear expression $\delta = \alpha(\rho(0) - C) + \beta$, where α, C, and β are functional- and basis set-dependent parameters and $\rho(0)$ is the calculated electron density at the Fe center.[41−43] The ligands' contribution to the EFG tensor was estimated by performing calculations on models for which the Fe(II) ions were replaced with Zn(II) ions.[44] The relaxed scans along the angle θ formed by the two planes defined by the OMO atoms, where O refers to the two oxygen atoms of a pin^F ligand and M to the 3d metal ion, were obtained by varying the dihedral angle between the two chelation rings and measuring θ for each individual geometry optimized structure. Specifically, θ was obtained from the OXXO dihedral angle with a value ≤90° where X are dummy atoms inserted at the center of the O−O distance of a selected pin^F ligand and the two O atoms of OXXO belong to two different pin^F ligands; see Scheme 3.

Scheme 3. Definition and Measurement of the Angle *θ*, which Quantifies the Angle Formed by the Two Chelating Pin^F Ligands[a]

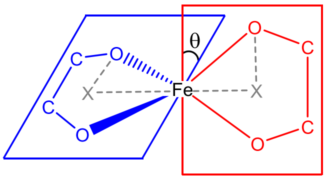

[a]Thus, θ is defined with the help of two dummy atoms, labeled X, which are inserted at the midpoint of the O−O distance of each pin^F ligand such that, numerically, θ is equal to the resulting OXXO dihedral angle.

3. RESULTS AND DISCUSSION

3.1. Synthesis and SCXRD. The $[Fe^{II}(pin^F)_2]^{2-}$ complexes shown in Figure 1 were synthesized according to a slightly modified version of a previously optimized route,[14] by generating $\{FeN''_2\}$ in situ (N″ = bis(trimethylsilyl amide)), and adding 2 equiv of KHpin^F. Previously reported magenta $\{K(DME)_2\}_2[Fe(pin^F)_2]$, **S**, was recrystallized from DME/hex solvent diffusion at −30 °C. $\{K(C222)\}_2[Fe(pin^F)_2]$, **S′**, was formed by adding 2 equiv of 2,2,2-cryptand, and blue crystals were grown out of layering a mixture of THF and DMSO with Et_2O. SCXRD structural determination parameters for **S′** are summarized in Tables S1 and S2. **S** is completely planar, with a τ_4 = 0 (0 = square planar, 1 = tetrahedral). The K^+ cations bridge the two pin^F ligands via two O atoms. In contrast to **S**, the anionic $[Fe(pin^F)_2]^{2-}$ moiety in **S′** is fully isolated from the K^+ cation, which is encapsulated by 2,2,2-cryptand. Whereas **S** has ideal square-planar geometry at Fe, **S′** contains two independent Fe centers in the asymmetric unit, each with half occupancy with τ_4 values of 0.37 and 0.27. Each Fe center sits on a twofold axis, and the Fe−O distances average 1.98(9) and 1.98(4) Å, consistent with **S**, in which the $Fe-O_{pinF}$ distances average bond lengths of 1.96(9) Å. Despite the different τ_4 values of **S′** and **S**, their average $Fe-O_{pinF}$ distances are surprisingly similar. Just as inferred from our computational study, this observation suggests the K^+ coordination on the alkoxide oxygen atoms does not play an important role in stabilizing a more planar $\{FeO_4\}$ site, *vide infra*.

3.2. High-Frequency EPR. *3.2.1. Overview.* HFEPR spectra of **S** and **T** were recorded at 5 and 20 K for frequencies ranging from 100 to 630 GHz. Selected spectra obtained for a neat powder of **S** are presented in Figure 2 and Figure S2. The changes induced by regrinding and dispersing the powder of **S** in mineral oil are illustrated by the corresponding 5 K, 203 GHz spectra presented in Figure S3. Similarly, Figure S4 presents spectra recorded at 5 K for a neat powder sample of **T** as well as some obtained at 20 K after regrinding and dispersing the powder in mineral oil. Figure S5 illustrates the temperature dependence of the experimental and theoretical 220.8 and 295.2 GHz spectra obtained for the neat powder sample of **T**. Finally, to illustrate the spectral contribution of a small ferric contaminant, Figure S6 presents a close-up of the $g \sim 2$ of the 20K, 220.8 GHz spectrum (Figure 3).

We have analyzed these spectra using the standard $S = 2$ spin Hamiltonian of eq 1 in which the first term accounts for the ZFS of the quintet ground spin state and the second for the electronic Zeeman interaction. All symbols in this equation have their conventional meaning.[45]

$$\hat{\mathbf{H}}_e = D\left[\left(\hat{S}_z^2 - 2\right) + \frac{E}{D}\left(\hat{S}_x^2 - \hat{S}_y^2\right)\right] + \beta_e \vec{\hat{\mathbf{S}}}\cdot\tilde{\mathbf{g}}\cdot\vec{\mathbf{B}} \tag{1}$$

Our analysis, summarized in Figure 2 for **S** and Figure 4 for **T**, used a two-pronged approach: first, we used the values of the resonant fields of all major signals to compile two-dimensional field vs frequency maps of energy gaps, informally known as "Florida plots" (shown at the right in Figures 2 and

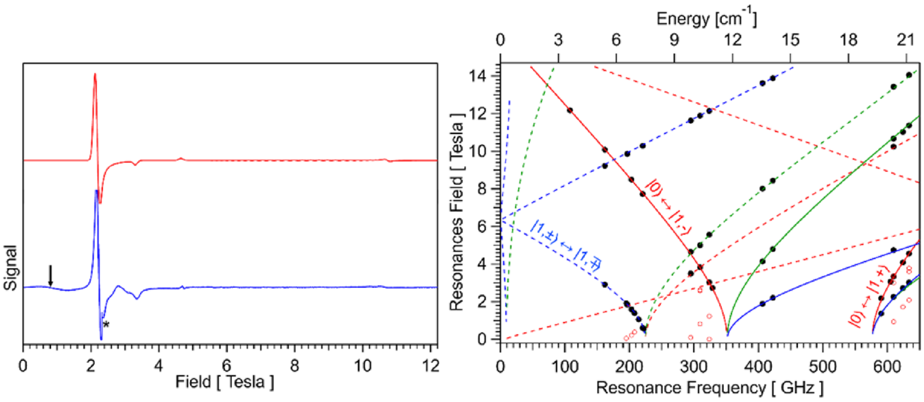

Figure 2. Left: experimental (blue) HFEPR spectrum recorded for **S** at 20 K using a microwave frequency of 609.6 GHz and theoretical curve (red) obtained using the parameters listed in Table 1. The black arrow highlights a resonance not accounted for in our analysis, and the feature marked by the asterisk is an instrumental artifact. Right: a field vs frequency plot in which black dots indicate the resonant fields and frequencies of the experimental resonances used to derive the spin Hamiltonian parameters of **S**. The red circles indicate the resonances not included in our analysis. The solid curves account for the theoretical dependencies of the ground-state resonances and the dashed curves of the excited state resonances. The red, blue, and green colors account for the *z*, *y*, and *x* molecular directions, respectively.

https://doi.org/10.1021/acs.inorgchem.3c03236
Inorg. Chem. 2024, 63, 2370−2387

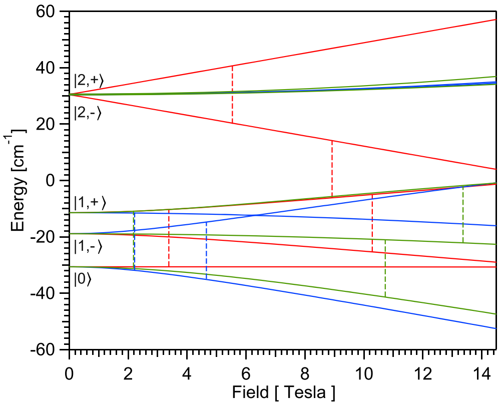

Figure 3. Energy levels obtained for a $S = 2$ spin system using the parameters derived from HFEPR for **S**, listed in Table 1. The red, blue, and green colors account for the z, y, and x molecular directions, respectively. The vertical lines highlight the resonant fields predicted for a microwave frequency of 609.6 GHz.

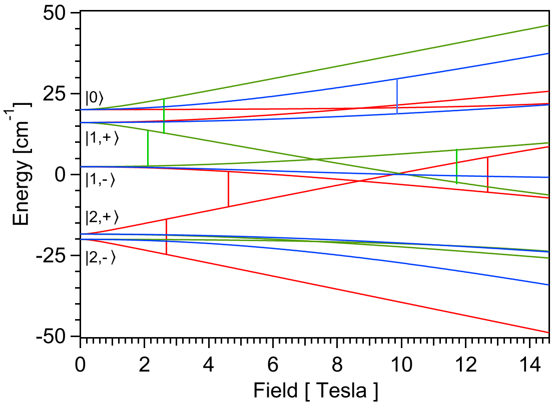

Figure 5. Energy levels obtained for a $S = 2$ spin system using the parameters derived from HFEPR for **T**, listed in Table 1. The red, green, and blue colors account for the z, y, and x molecular directions, respectively. The vertical lines highlight the resonant fields predicted for a microwave frequency of 324 GHz.

4), and second, we performed extensive simulations of the individual spectra included in our analysis.[46] The evaluation of the field vs frequency plots provided us with the best estimates of the experimental ZFS and **g** tensors, and the spectral simulations (one example each at the left of Figures 2 and 4) allowed us to rationalize the origin of the observed resonances. In this analysis, we used as initial parameters those first derived from the field-dependent Mössbauer spectra, which, although quite robust, due to technical limitations are not as accurate as those provided by HFEPR. Inspection of the right sides of Figures 2 and 4 shows that, upon some refinement, these parameters have allowed us to account for most of the observed resonances (Figure 5).

*3.2.2. HFEPR Spectra of **S**.* To determine the ZFS and g tensors of **S**, we have recorded a series of HFEPR spectra for a neat, ground powder sample at frequencies ranging from 108 to 643 GHz, at 5 and 20 K (Figure S2). Interestingly, these spectra showed a large number of features, some of which were attributed to randomly oriented single crystals, which generate narrow but intense resonances in imperfectly ground and/or magnetically torqued powder samples. This could be seen as a "grass pattern" in some of the high-frequency spectra such as those obtained at ~400 GHz (Figure S2). To eliminate these unwanted spectral artifacts, we reground the sample and dispersed them in a chemically inert mineral oil, Nujol. However, inspection of Figure S3 shows that this treatment was only partially successful. Nevertheless, despite these shortcomings, we were able to successfully rationalize most of the genuine powder-type resonances observed for these spectra, *vide infra*.

The field vs frequency plot obtained for **S**, Figure 2 right, reveals that the spectra obtained for frequencies below 162 GHz did not provide any useful information. Moreover, most of the spectra recorded at ~200 GHz are dominated by a single low field, relatively intense resonance. A notable feature of this absorption is that it moves to lower resonant fields when the microwave frequency is increased. Thus, in this case, increasing the strength of the applied field leads to a decrease in the energy splitting of the levels between which the resonance takes place and therefore to a lower resonant frequency. Inspection of the energy level diagrams presented in Figure 3 shows that this resonance may be traced to a transition occurring at the y orientation, between the levels of the $|1,\pm\rangle$ excited quasi-doublet. Therefore, we observe a $|1,\pm\rangle \leftrightarrow |1,\pm\rangle$

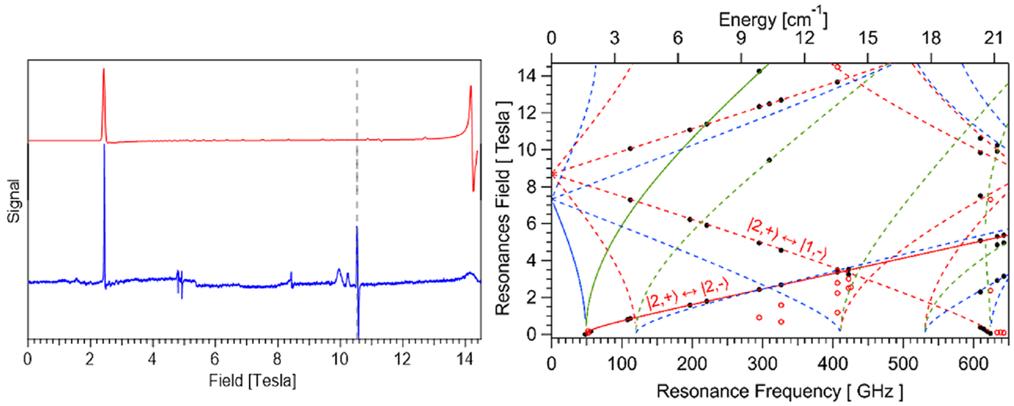

Figure 4. Left: experimental (blue) HFEPR spectrum recorded at 5 K for **T** using a microwave frequency of 295.2 GHz and theoretical curve (red) obtained using the parameters listed in Table 1. The dashed vertical line marks the location of the $g = 2.0023$. Right: the black dots present the field vs frequency location of the experimental resonances. The red circles indicate resonances not included in our analysis. The solid curves account for the theoretical dependencies of the ground-state resonances and the dashed curves of the excited-state resonances. The red, green, and blue colors account for the z, y, and x molecular directions, respectively.

https://doi.org/10.1021/acs.inorgchem.3c03236
Inorg. Chem. 2024, 63, 2370−2387

Table 1. Spin Hamiltonian Parameters of S and T, Determined from the HFEPR Spectra and Comparison with Other Relevant Complexes

compound	D [cm^{-1}]	E [cm^{-1}]	E/D	g-tensor			ref.
				g_x	g_y	g_z	
S	15.17(1)	1.246(1)	0.08	2.090(3)	2.167(3)	1.99(1)	[e]
$(CF_3ONO)FeCl$[a]	17.4	2.43	0.14	2.19	2.18	2.04	18
T	−9.16(1)	−2.26(1)	0.24	2.17(1)	2.18(1)	2.191(3)	[e]
$[Fe(SR)_3]^-$[b]	10.2(5)[d]	2.04	0.20		*not reported*		25
$Li(THF)_2Fe(SR)_3$[c]	14(3)[d]	3.5	0.25				

[a] CF_3ONO is the pincer-type ligand 2,2′(azanediylbis(2,1-phenylene)bis(1,1,1,3,3,3-hexa-fluoro-propan-2-olate). The second coordination sphere of this complex is stabilized by two Li^+ ions. Parameters derived from HFEPR and field-dependent Mössbauer studies. [b] The complete formula is $Ph_4P[Fe(SR)_3]\cdot 2MeCN\cdot C_7H_8$, where R = C_6H_2-2,4,6-$^tBu_3$. Parameters derived from field-dependent Mössbauer studies. [c] The complete formula is $[Li(THF)_2Fe(SR)_3]\cdot 1/2C_6H_{14}$ where R = C_6H_2-2,4,6-$^tBu_3$. Parameters derived from field-dependent Mössbauer studies. [d] The values in the round brackets provide estimated uncertainties of the last significant digit. [e] This work. Parameters derived from HFEPR and field-dependent Mössbauer studies.

transition, which in zero field has an energy gap of 6E. Consequently, the zero-field crossing observed at ∼224 GHz suggests that *S* has a rhombic ZFS parameter E = 1.25 cm^{-1}. Interestingly, the frequency vs field dependence inferred for this resonance "bounces" off the field axis at 6.2 T, meaning that these levels intersect at this field value such that a transition between the same levels at the y orientation is also observed for fields >6.2 T and frequencies up to 420 GHz. There is another zero-field crossing at ∼575 GHz, which may be assigned to the $|0\rangle \leftrightarrow |1,+\rangle$ resonance. This transition has a ZFS of $D+3E$ allowing us to estimate the D parameter 575 GHz − 112 GHz = 463 GHz or 15.4 cm^{-1}. Further parameter refinement was achieved by fitting the experimental resonances in Figure 2. Finally, the ground-state character of these resonances and therefore the sign of D were further confirmed by simulations of individual spectra such as that presented in Figure 2.

In addition to the experimental resonances, shown as black dots in Figure 2, used to derive the spin Hamiltonian parameters of **S** listed in Table 1, we have also observed a number of less prominent absorptions, which were not rationalized by these parameters, indicated as red dots in Figure 2. A representative example is highlighted by the vertical black arrow of Figure 2. The zero-field Mössbauer spectra recorded for this sample shown in Figure 6 and Figure S8a demonstrate that either these putative contaminants cannot be distinguished by Mössbauer spectroscopy or that they account for less than 2% of the Fe present in the sample. Interestingly, these species exhibit zero-field transitions at 197, 298, 329, and 600 GHz. If we assume that for one of these species $D + 3E$ = 600 GHz and $D - 3E$ = 329 GHz, we infer that its ZFS parameters are $D \sim 15.5$ cm^{-1} and $E/D \sim 0.1$. Although the other zero-field transitions lead to smaller D values, they are still indistinguishable from one another by field-dependent Mössbauer and are comparable to that obtained for **S**. This observation suggests that these species incorporate structurally different but chemically analogous Fe(II) sites such as the different conformers for the anions in $\{K(C222)\}_2[Fe^{II}(pin^F)_2]$, **S′**.

*3.2.3. HFEPR Spectra of **T**.* The features in the spectra recorded for **T** are rather sparse with only a handful of clearly identifiable absorptions. However, most of these spectra exhibit a relatively intense low-field resonance with an effective g value that changes from ∼10.2 at 98 GHz to ∼8.5 at 634 GHz (see Figure 4 and Figure S4. For an S = 2 spin system, such g values are typically observed for signals which originate from a transition within the $|2,\pm\rangle$ quasi-doublet.[47] When the ZFS of this quasi-doublet, $\delta_{ZFS} \cong 3D(E/D)^2$, is of the order of ∼0.3 cm^{-1}, a resonance may be observed for systems with negative D at X-band EPR using a parallel microwave polarization mode. Nevertheless, because in this case $\delta_{ZFS} \sim$ 1.6 cm^{-1}, no X-band EPR spectra of this kind can be observed for **T** despite its negative D parameter, *vide infra*. Inspection of Figure 4 shows that a frequency of at least 48 GHz is needed to detect this transition. The selection rule that applies in this case, $\Delta m_s = 0$, indicates that a transition is observed only when B_1, the oscillating magnetic component of the microwave field, has a nonzero projection along the molecular z-axis.

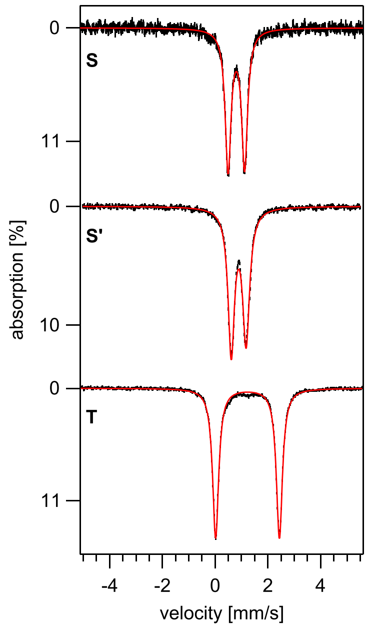

Figure 6. Zero-field Mössbauer spectra recorded at 4 K for **S** (top), **S′** (middle), and **T** (bottom). The solid red lines are theoretical spectra obtained using a Lorentzian line shape with a line width Γ = 0.27 mm/s for **S**, Γ = 0.29/0.32 mm/s for **S′**, and Γ = 0.28 mm/s for **T** and the parameters listed in Table 2.

In contrast to standard EPR spectrometers, the instrument used in this work did not incorporate a resonant cavity. Because of this technical feature, the microwave modes are disordered such that the parallel and perpendicular polarizations are both present. As a result, we routinely observe "forbidden" transitions. Furthermore, the corresponding transition probability is determined by the $\langle 2,+|\hat{S}_z|2,-\rangle$ matrix

Table 2. Zero-Field Mössbauer Parameters of S, S′, and T as well as of Other Relevant Iron Complexes or Iron-Containing Materials

compound	Fe site geometry[a]	T [K]	δ [mm/s]	ΔE_Q [mm/s]	ref.
α-Fe(II) Mordenite	SP	293[c]	0.89	0.55	10
$\{K(DME)_2\}_2[Fe(pin^F)_2]$, **S**	SP	4.2	0.807(3)	0.626(4)	[b]
$\{K(C222)\}_2[Fe(pin^F)_2]$, **S′**	SP	4.3	0.895(4)	0.564(4)	[b]
$(CF_3ONO)FeCl$	SP	4.2	0.82(1)	0.45(1)	18
$[Li_2(THF)_4Fe(O(SiPh_2O)_2)_2]$	SP	13−120	0.87	0.53	22
$\{K(18C6)\}[Fe(OC_4F_9)_3]$, **T**	TP	4.2	1.231(3)	2.418(2)	[b]
$[Na(DME)Fe(OSiPh_3)_3]$	TP	15	0.74	0.95	49
$[Fe(SR)_3]^-$	TP	4.2	0.56(1)	0.83(2)	25
$Li(THF)_2Fe(SR)_3$	TP	4.2	0.60(1)	0.87(2)	25

[a] SP = square planar, TP = trigonal planar. [b] This work. [c] Room temperature.

element, which is proportional to the mixing of the $|S,m_s\rangle = |2,\pm2\rangle$ spin sublevels with $|2,0\rangle$. Since for $E = 0$ this matrix element is null, the persistence of this mixing in an applied field is determined by the magnitude of the ZFS parameter E. Therefore, the observation of this resonance at large field and frequencies, even as large as 5 T and 600 GHz, demonstrates that **T** must have a sizable E/D. Inspection of Figure S5 shows that the temperature-dependent behavior of this absorption is indicative of a ground-state resonance suggesting that D is negative. Most importantly, the review of the field vs frequency plot, right side of Figure 4, obtained for **T** suggests that this resonance "crosses" the $B = 0$ axis at ∼48 GHz, which provides us with a direct measure of the $|2,\pm\rangle$ ground quasi-doublet's ZFS, namely, $\delta_{ZFS} \sim 1.6$ cm^{-1}. Interestingly, another zero-field crossing is observed at ∼620 GHz, which can be traced to an inter (quasi) doublets $|2,\pm\rangle \leftrightarrow |1,\pm\rangle$ transition. This resonance "moves against" frequency, that is, increasing the microwave frequency leads to a lower resonant field, which demonstrates that the splitting of the two levels between which the transition takes place decreases with increasing strength of the applied field. Therefore, we may assign this absorption to the $|2,+\rangle \leftrightarrow |1,-\rangle$ transition, which has a ZFS $\Delta = 3D - 3E$ (see Figure 5 for the labels of the spin levels). While a first estimate of the ZFS parameters may be derived from these energy gaps, $D \sim -9$ cm^{-1} and $E \sim 2$ cm^{-1}, which are essentially identical to the parameters derived from the analysis of the field-dependent Mössbauer spectra, the values listed in Table 1 were obtained by fitting the field and frequency dependence of the resonances indicated as black dots in Figure 4, right.

A surprising feature of the field vs frequency plot obtained for **T** is that most absorptions identified for this species are z-type resonances. This result is due not only to the peculiar properties of this spin system but also to the field-induced alignment, "torquing" of the microcrystalline powder. This alignment allows the z resonances to be more easily detected. This torquing likely occurred during the acquisition of the first HFEPR spectrum obtained for the neat powder sample. Thus, inspection of Figures S4 and S5 shows that nearly all resonances observed for the neat powder not only are very intense but also cross the baseline, which is expected in single-crystal spectra but not in powders with randomly distributed molecular orientations. The applied magnetic field tends to orient the individual crystals such that their easy axis, which for negative D typically is the molecular z-axis becomes parallel to the applied field. The relative intensities of the resonances associated with **T** may be judged from their comparison with those clustered around $g \sim 2.00$. These resonances originate from a high-spin ferric contaminant, are not influenced by torquing, and exhibit normal powder shape (Figure S4). A theoretical fit of an $S = 5/2$ system in this region is shown in Figure S6. To mitigate this experimental artifact, just like for **S**, we reground the polycrystalline powder and dispersed it in Nujol. Upon freezing, the oil locks the individual grains in place and prevents the field-induced reorientation. The HFEPR spectra of the immobilized sample exhibit a characteristic powder pattern with the z resonances, including the high-g transition within the $|2,\pm\rangle$ quasi-doublet, not crossing the baseline. Their intensity is drastically reduced, and additional resonances, along y and x axes, can be clearly identified (see Figure S4).

In addition to the resonances clustered around $g \sim 2$, there are several other features not rationalized by the parameters we determined for **T**. These absorptions are most conspicuous at low field for the spectra recorded at ∼300 GHz and are shown using red circles in the field vs frequency plot of Figure 4. Interestingly, analogous to the contaminants observed for **S**, these features most likely originate from a high-spin Fe(II) species with a large positive ZFS, $D \sim 14.8$ cm^{-1} and $E/D \sim 0.15$. Our theoretical analysis suggests that such parameters may be observed for a species derived from **T** for which the K$^+$ cation is displaced from the second coordination sphere of the Fe(II) ion. The loss of the alkali metal cation not only causes the symmetry of the trigonal transition metal site to change from C_{2v} to C_{3v} but also induces a switch in the sign of D, *vide infra*.

3.3. ^{57}Fe Mössbauer Spectroscopy.

3.3.1. Zero-Field Spectra. The zero-field spectra recorded for **S**/**S′** and **T** consist of single, well-defined quadrupole doublets, which account for >98% of the iron contained in their corresponding samples. The quadrupole doublet of **S** exhibits relatively narrow line widths, $\Gamma = 0.27$ mm/s, which suggests that the Fe site of **S** is structurally homogeneous. Furthermore, at 4.2 K, this doublet has an isomer shift of $\delta = 0.807(3)$ mm/s and a quadrupole splitting $\Delta E_Q = 0.626(4)$ mm/s (see Figure 6 top). While this isomer shift value is typical of high-spin Fe(II) ions, the ΔE_Q is unusually small for such chemical species.[48] Nevertheless, the magnitude of this parameter is similar to that of other high-spin, square-planar, Fe(II) compounds including $[Li_2(THF)_2(CF_3ONO)FeCl]$ (see Scheme 1), reported by Pascualini et al., which was also characterized by field-dependent Mössbauer and HFEPR (see Tables 1, 2, and 3).[18] Similarly, for **S′**, we observed a slightly asymmetric quadrupole doublet characterized by an isomer shift $\delta = 0.895(4)$ mm/s and a quadrupole splitting $\Delta E_Q = 0.564(4)$ mm/s (see Figure 6 middle). Although the linewidths of these resonances are slightly larger than those of **S**, $\Gamma_{L/R} = 0.29/0.32$

Table 3. Hyperfine Structure Parameters Obtained from the Analysis of the Field-Dependent Spectra Obtained for S/S′ and T and of Selected Analogous Complexes[a]

				EFG tensor rotation						
compound	δ[b] [mm/s]	ΔE_Q[b] [mm/s]	η	α [°]	β [°]	γ [°]	$A_x/\beta_n g_n$[T]	$A_y/\beta_n g_n$ [T]	$A_z/\beta_n g_n$ [T]	**ref.**
S	0.807	0.626	0.5(1)	18	30	0	−18.4(5)	−13.4(6)	−31(1)	[e]
S′ site a	0.895	0.564	0.0	0	90	0	−9.5	−14.6	−35	[e]
site b	0.895	−0.564	0.2	0	90	90	−6.1	−12.1	−35	[e]
$(CF_3ONO)FeCl$	0.82	−0.45	0.6(2)	0	90(45)	90(90)	−17(1)	−13(1)	−30(2)	18
T	1.231	−2.418[c]	0.82(10)[c]	90	90	90	−18.5(5)[e]	−24.5(5)[e]	−3.6(2)[e]	[e]
$[Fe(SR)_3]^-$	0.56	−0.83	0	0	0	0	−5.5(4)	−5.5(4)	−21.2(10.2)	25
$Li(THF)_2Fe(SR)_3$	0.60	−0.87	0.93(7)	60	0	0	−2.8[d]	+3.3[d]	−26(3)[d]	25

[a] The ZFS and g tensors of **S** and **T** were determined from the analysis of the HFEPR spectra and are presented in Table 1. Where available, the values in the round brackets provide estimated uncertainties of the last significant digits. [b] Values observed at 4.2 K. [c] This solution may also be represented using $\Delta E_Q = 2.418$, $\alpha = \beta = \gamma = 0°$ and the nonstandard $\eta = 1.2(1)$ value. [d] The hyperfine splitting tensor A is rotated from the reference frame of the ZFS by $\alpha_A = 60°$, $\beta_A = \gamma_A = 0°$. The magnitudes of A_x and A_y depend on the choice of D and the rotation of the EFG tensor; however, they are both smaller than 3.4 T. [e] This work.

mm/s, they are still fairly typical of those observed for chemically homogeneous Fe(II) sites. Nonetheless, we have attempted to deconvolute the individual spectral components associated with the two crystallographically distinct sites of **S′** using both a nested and an intercalated arrangement of two doublets (see Figure S7). However, inspection of the parameters derived from these simulations, listed in Table S4, shows that this effort was essentially unsuccessful, that the two sites of **S′** cannot be distinguished in the zero-field Mössbauer spectra. Interestingly, the small ΔE_Q of these compounds originates from the competition between two opposite contributions to the electric field gradient (EFG) tensor. The large valence contribution generated by the doubly occupied $3d_{z^2}$ orbital is nearly quenched by the ligand contribution generated by the negatively charged ligands located in the plane of the molecule, *vide infra*.

We anticipated that the combination of factors responsible for the unusually small quadrupole splitting of **S**/**S′** would also be operative for **T** such that we would observe a similar set of parameter values. However, while the quadrupole doublet of **T**, similarly to that of **S**, exhibits narrow line widths indicative of a chemically pure, structurally homogeneous species and is characterized by $\delta = 1.231(3)$ mm/s, the $\Delta E_Q = 2.418(2)$ mm/s of **T** is much larger than that of **S**/**S′** (see Figure 6 bottom). Moreover, inspection of Table 2 shows that the ΔE_Q of **T** is also larger than those obtained for the analogous thiolate-supported, three-coordinate Fe(II) complexes (see Table 2). The analysis of the latter compounds showed that just like for square-planar Fe(II) compounds, their low quadrupole splitting is indicative of a z^2-type ground state. Consequently, the large ΔE_Q of **T** and its negative ZFS (*vide supra*) are, most likely, indicative of a non-z^2 ground state.

The isomer shifts of **S**/**S′** and **T** exhibit only a slight temperature dependence; at 180 K, their values are 0.02−0.03 mm/s lower than those observed at 4.2 K (see Tables S5, S6, and Figures S8−S10). This change is typical and originates from a second-order Doppler effect.[48] While the quadrupole splitting of **S**/**S′** is essentially temperature-independent decreasing by less than 0.03 mm/s from 4.2 to 180 K, the change observed for **T** is nearly 10 times as large such that at 180 K, $\Delta E_Q = 2.13(2)$ mm/s. These trends likely indicate that while **S**/**S′** have thermally isolated orbital ground states, **T** exhibits a low-lying excited orbital state, which, even at 180 K, acquires a sizable Boltzmann population.

3.3.2. Field-Dependent Spectra. The field-dependent Mössbauer spectra recorded for **S**/**S′** and **T** have been analyzed using the standard spin Hamiltonian of eq 2.[50] This expression was obtained by augmenting the electronic spin Hamiltonian of eq 1 with terms that account for the nuclear hyperfine interactions of ^{57}Fe nuclei and which are detailed in eq 3.

$$\hat{\mathbf{H}} = \hat{\mathbf{H}}_{\mathrm{e}} + \hat{\mathbf{H}}_{\mathrm{hf}} \tag{2}$$

$$\hat{\mathbf{H}}_{\mathrm{hf}} = \delta + \vec{\hat{\mathbf{I}}}\cdot\widetilde{\mathbf{P}}\cdot\vec{\hat{\mathbf{I}}} + \vec{\hat{\mathbf{S}}}\cdot\widetilde{\boldsymbol{A}}\cdot\vec{\hat{\mathbf{I}}} - \beta_n g_n \vec{\hat{\mathbf{S}}}\cdot\vec{\hat{\mathbf{I}}} \tag{3}$$

$$\vec{\hat{\mathbf{I}}}\cdot\widetilde{\mathbf{P}}\cdot\vec{\hat{\mathbf{I}}} = \frac{eQ}{12}V_{ZZ}[3\hat{I}_{ZZ} - I(I+1) + \eta(\hat{I}_{XX} - \hat{I}_{YY})] \tag{4}$$

From left to right, the individual terms of eq 3 account for the isomer shift (electric monopole), electric quadrupole interaction, hyperfine coupling, and nuclear Zeeman interaction, respectively. Equation 4 allows us to connect the individual tensor components V_{ZZ}, V_{XX}, and V_{YY} of the EFG tensor $\widetilde{\mathbf{P}}$ with the quadrupole splitting, $\Delta E_Q = (eQV_{ZZ}/2)\sqrt{1+\eta^2/3}$, and the EFG asymmetry parameter, $\eta = (V_{XX} - V_{YY})/V_{ZZ}$. The relative orientation of the EFG and A tensors with respect to the ZFS tensor of eq 2, which provided the reference frame, was described using a standard set of Euler angles $\{R_z(\alpha) \to R_y(\beta) \to R_z(\gamma)\}$.

*3.3.3. Field-Dependent Spectra of **S**.* Based on the similarity of the square-planar structure and zero-field Mössbauer spectra of **S** with those of $[(CF_3ONO)FeCl]$, we anticipated a positive D and an axial ZFS tensor ($E/D \sim 0$).[18] This assumption was readily validated by our spectral simulations. Inspection of Figure 7 and Figure S11 shows that at 4.2 K, the applied field leads to a gradual development of a field-induced hyperfine splitting, which fails to reach a saturation value even at 8 T. This behavior is indicative of a positive D value, which leads to a $|S, m\rangle = |2,0\rangle \approx |0\rangle$ ground state. In this case, the applied field mixes the excited $|1, \pm\rangle = (|2, 1\rangle \pm |2, -1\rangle)/\sqrt{2}$. spin sublevels into the ground state leading to spin expectation values such that $\langle\hat{S}_z\rangle \approx 0$ and $\langle\hat{S}_x\rangle$, $\langle\hat{S}_y\rangle$ are finite, approximately −1.6 at 8 T (see Figure S13). Consequently, the low-temperature data are

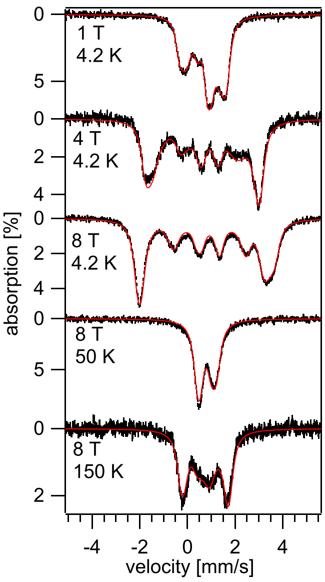

Figure 7. Field- and temperature-dependent Mössbauer spectra recorded for **S**. The solid red lines are simulations obtained using eq 2, and the parameters listed in Tables 1 and 2. The complete set of field-dependent spectra included in our analysis is presented in Figures S11 and S12.

sensitive to A_x, A_y, and D but they are independent of A_z. The latter parameter was determined from the spectra recorded at $T \geq 20$ K (see Figure S12), for which the $|1, -\rangle$ spin sublevel acquires a sizable Boltzmann population and leads to a significant contribution to $\langle \hat{S}_z \rangle_{\mathrm{th}}$. Thus, the hyperfine splitting pattern of the field-dependent spectra is determined by the vectorial sum of the applied magnetic field and the internal magnetic field, $\vec{\mathbf{B}}_{\mathrm{int}} = -\langle \hat{\vec{\mathbf{S}}} \rangle \cdot \tilde{\mathbf{A}}/g_n\beta_n$, where $\langle \hat{\vec{\mathbf{S}}} \rangle$ is the spin expectation value.[50]

All 4.2 K spectra recorded for complex **S** were simulated assuming a slow relaxation rate of the electronic spin. The spectra recorded at higher temperatures were obtained assuming a fast relaxation regime for which the $\langle \hat{\vec{\mathbf{S}}} \rangle$ is averaged over all thermally accessible spin sublevels, labeled $\langle \hat{\vec{\mathbf{S}}} \rangle_{\mathrm{th}}$. At high temperatures, for which $k_BT \gg D$, the $\langle \hat{\vec{\mathbf{S}}} \rangle_{\mathrm{th}}$ is inversely proportional to the temperature such that the internal field follows Curie's law.[51] Under these conditions, $\vec{\mathbf{B}}_{\mathrm{int}}$ is virtually independent of the ZFS parameters D and E/D, and the simulations of these spectra provided the magnitude of the A tensor components and of η, the asymmetry parameter of the EFG tensor. The size of the ZFS parameter D was first estimated from the spectra obtained at intermediate temperatures, particularly those recorded between 10 and 80 K. The parameter values listed in Tables 1–3 were derived from the combined analysis of the field-dependent Mössbauer and HFEPR spectra and were used to generate all theoretical spectra included in this manuscript. In contrast to the theoretical EPR spectra, the simulated Mössbauer spectra are not as sensitive to minute changes of the ZFS parameter values. Consequently, the ZFS parameters obtained using Mössbauer spectroscopy are more robust; however, their values are not as precise as those obtained from EPR.

3.3.4. *Field-Dependent Spectra of* ***S′***.

While the magnitude of the hyperfine splitting pattern of the field-dependent spectra obtained for **S′** is similar to that of **S**, the corresponding spectral shapes are quite different (see Figure 8 and Figures S14 and S15). In particular, the 4.3 K spectra exhibit relatively few distinguishing features such that, except for the two low-energy features of the 4.3 K, 6–8 T spectra, the individual spectral components associated with the two sites overlap and cannot be distinguished from one another (see Figure S14). Considering our inability to differentiate the individual spectral components associated with two sites and the large number of parameters required to simulate each component, up to 26 parameters per site, to rationalize these field-dependent spectra, we have introduced several simplifications. Thus, we have employed the ZFS and $\boldsymbol{g}$ tensors derived from the HFEPR studies of **S**. In addition, we have kept the magnitude of the zero-field Mössbauer parameters of the two sites the same. We found that even with these limitations most of the field-dependent spectra of **S′**, shown in Figures S14 and S15, may be reproduced fairly well, using individual $\boldsymbol{A}$ tensors that are clearly reminiscent of that obtained for **S** (see Table 3).

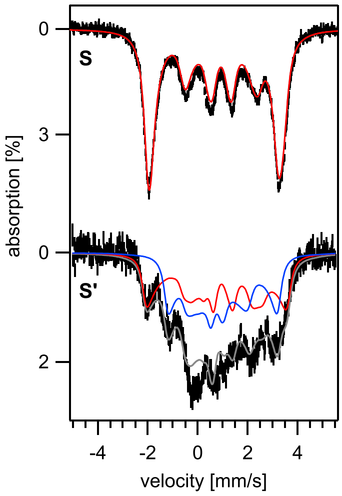

Figure 8. Comparison of the 4 K, 6 T Mössbauer spectra recorded for **S** (top) and **S′** (bottom). The theoretical spectra of **S′** were obtained using the parameters listed in Tables 1–3 for site a (red) and site b (blue). The complete set of field-dependent spectra acquired for **S′** are presented in Figures S14 and S15.

3.3.5. *Field-Dependent Spectra of* ***T***.

The field-dependent spectra recorded at 4.2 K for **T**, some of which are shown in Figure 9, exhibit two notable features. First, the spectra recorded at 7–8 T exhibit an unusual triangular shape. In this case, the individual resonances that are typically observed at high fields merge into two broad absorption lines, which are essentially devoid of prominent features. Although such spectral shapes are uncommon, they have been occasionally observed for $S = 1/2$ species that have highly anisotropic A tensors.[52] Second, analysis of the low-field ($B \leq 2$ T) spectra demonstrates a field-induced change in the relaxation rate of the electronic spin from fast ($\omega \geq 10^{10}$ Hz) to slow ($\omega \leq 10^{7}$ Hz) when compared to the Mössbauer time scale ($\tau_M \sim 10^{-9}$ s) (see Figures S16 and S17). Even though a comparable behavior is often described when AC magnetometry is employed to investigate the spin-dynamics of molecular magnets, due to the considerably shorter time scale, such effects are rarely observed using Mössbauer spectroscopy.[53,54] Interestingly, the orientation-dependent change in the relaxation rate observed for four-coordinate LFe$^{\mathrm{II}}$(μ-Cl)$_2$Li-

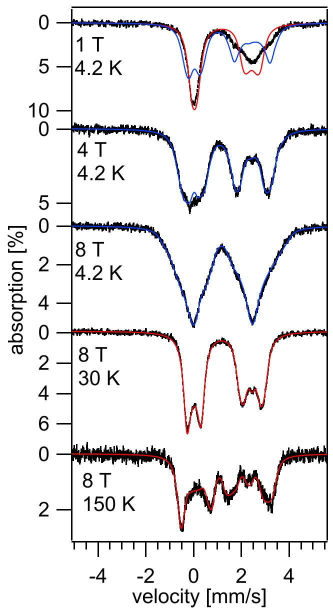

Figure 9. Field- and temperature-dependent Mössbauer spectra recorded for **T**. The solid lines are simulations obtained using eq 4 and the parameters listed in Tables 1 and 2. For the complete data set used to derive these parameters, see Figures S12−S15. While the theoretical spectra shown in blue were obtained assuming a slow relaxation regime, those shown in red were obtained for a fast relaxation regime of the electronic spin.

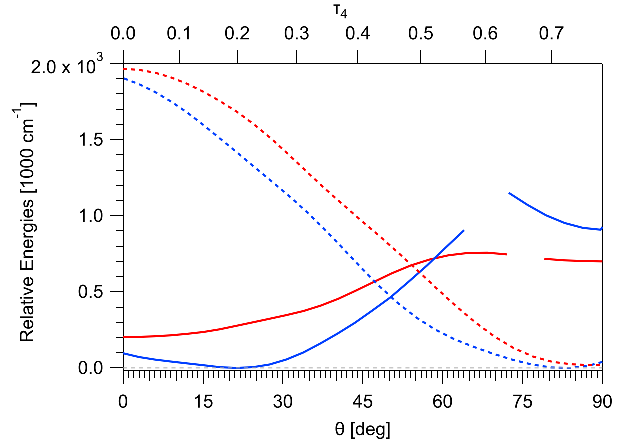

Figure 10. Potential energy curves obtained for the $\delta\lambda$ (red) and $\delta\delta$ (blue) isomers of $[\mathrm{M(pin^F)_2}]^{2-}$ where the curves obtained for Fe(II) are shown using solid and those for Zn(II) using dashed lines. These curves were obtained from relaxed scans performed at the BP86/def2-TZVPP level of theory; see text. The τ_4 values of the top axis are reported with respect to the potential obtained for $\delta\lambda$-$[\mathrm{Fe(pin^F)_2}]^{2-}$. The gaps of the $[\mathrm{Fe(pin^F)_2}]^{2-}$ traces correspond to points for which the SCF did not converge.

$(\mathrm{THF})_2$, where L is a sterically encumbered β-diketiminate ligand, leads to spectra with similar features as those observed for **T**.[55] More recently, a similar behavior has also been observed for two iron(II) complexes supported by dichalcogenidoimidodiphosphinato ligands.[53] Thus, inspection of Figure S16 shows that for fields below 0.5 T, the spectra are well simulated assuming a fast relaxation regime. However, for $B = 1{-}2$ T, the high energy peak, which for these simulations is the most sensitive to A_z, has a hyperfine splitting that is considerably larger than that expected for a fast relaxation regime. Thus, the magnitude of this splitting is well reproduced when a slow relaxation regime is assumed (see Figure 9 and Figures S16 and S17). As the strength of the applied field increases above 3 T, the experimental spectra are well reproduced by assuming a slow relaxation rate (Figure 10). Nevertheless, at 4.2 K for larger field values, $B \geq 5$ T, for which the spin expectation value of the lowest spin sublevel reaches its saturation value and is essentially equal to the thermally averaged spin expectation values, $\langle 2,-|\hat{S}_z|2,-\rangle \approx \langle \hat{S}_z\rangle_{\mathrm{th}} \approx -2$, the shape of the theoretical spectra is independent of the relaxation rate (see Figures S18 and S19). The hyperfine coupling parameters derived from the analysis of the field-dependent spectra are presented in Table 3. Moreover, the entire set of field-dependent spectra and the corresponding simulations are presented in Figures S16−S19.

3.4. Theoretical and Computational Studies.

3.4.1. Overview. Our computational investigation suggests that the distortion of the two Fe(II) sites of **S′** with $\tau_4 = 0.27$ and 0.37,[56] when compared to a perfectly planar site of **S**, $\tau_4 = 0.00$, is primarily caused by the change in the conformation of the two Fe-pin$^\mathrm{F}$ chelate rings (see Scheme 2). Although the $C222$ cryptand blocks the K$^+$ ions from interacting with the $[\mathrm{FeO_4}]$ sites, the asymmetric unit of **S′** incorporates two distinct Fe ions each chelated by two pin$^\mathrm{F}$ ligands, which adopt a similar $\delta\delta$ conformation (see Figure S1). In contrast, for **S**, we observe only one $\delta\lambda$-$[\mathrm{Fe(pin^F)_2}]^{2-}$ anion (see Table S3). Nevertheless, the main effect of this distortion is to lower the energy of the $|xy\rangle$ state (see Figure 11 and Figure S22). Since this state has little to no influence on the spin−orbit interactions, just as observed experimentally, the magnetic anisotropies and spectroscopic behavior of **S** and **S′** are quite similar. While the electronic structure and geometry of **T** can only be rationalized by considering the strong interaction of the $[\mathrm{Fe(OC_4F_9)}]^-$ complex anion with the $\{\mathrm{K(18C6)}\}^+$ cation, the countercations of **S**/**S′** have virtually no influence on the electronic structure and geometries of their Fe(II) sites. In fact, our computational investigation suggests that despite the fact the K$^+$ ions of **S** are bound directly to the oxygen atoms of the

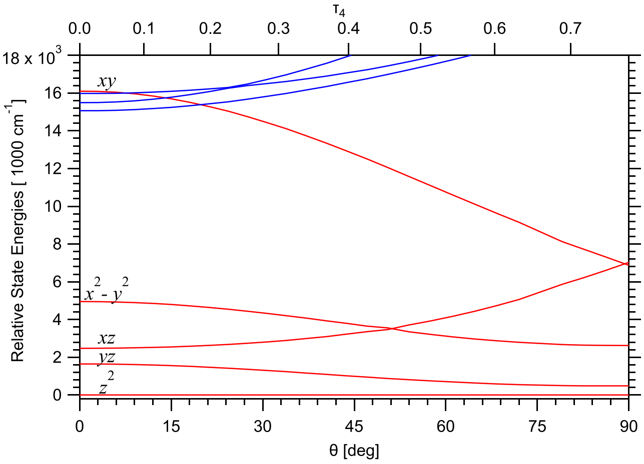

Figure 11. Relative energies of the five quintet states, shown in red, and of the three lowest triplet states, represented in blue, predicted by CASSCF(5,6) calculations which considered all five quintet and all 35 triplet states performed on the geometry optimized structures derived from the BP86/def2-TZVPP relaxed scan along θ for $\delta\lambda$-[Fe(pinF)$_2$]$^{2-}$. The labels of the quintet states refer to the states of the approximately square planar geometry (C_{2h}), at $\theta = 0°$.

$[FeO_4]$ moiety, their main influence on the electronic structure of the Fe(II) site is to lower the energy of the $|yz\rangle$ state by ~400 cm^{-1} (see Figure S22).

3.4.2. Factors that Influence the Geometries of ***S/S′***. Our geometry optimizations performed using DFT on structural models of **S** indicate that the excision of the $\{K(DME)_2\}^+$ cations does not induce a decrease in the planarity of the $[FeO_4]$ structural motif. Thus, these calculations suggest that the inclusion of the K^+ ions in the second coordination sphere of the Fe(II) site does not constitute a prerequisite for the stabilization of a square planar geometry. Experimentally, this conclusion is corroborated by the structure of $(Me_4N)_2[Fe(pin^F)_2]\cdot 2CH_3CN$, which incorporates a perfectly planar $[FeO_4]$ moiety but lacks a direct interaction between the pin^F ligands and alkali ions.[14] Additionally, our reinvestigation of the potential energy surface along the angle θ formed by the two pin^F ligands (see Scheme 3), obtained from a relaxed scan performed at the BP86/def2-TZVPP level of theory, also suggests that a planar $[FeO_4]$ geometry corresponds to a global minimum.

However, inspection of Figure 10 shows that this potential is quite shallow, with a maximum of ~550 cm^{-1} observed at $\tau_4 \sim 0.55$, and that a second local minimum is observed at $\theta \sim 90°$, $\tau_4 \sim 0.78$. This higher energy local minimum is 495 cm^{-1}, ~1.4 kcal/mol, above that observed at ~0° for the planar structure. Consequently, this scan indicates that the Fe(II) site of the $[Fe(pin^F)_2]^{2-}$ anion may be easily distorted, which might explain the distortions observed for the two Fe sites of **S′** and that of $PPN[Li(MeOH)_4][Fe(pin^F)_2]$.[17] Then again, we find that we obtain a global minimum at ~0° only when the two ligands of $[Fe(pin^F)_2]^{2-}$ adopt a $\delta\lambda$ conformation, such as that observed for **S** and $(Me_4N)_2[Fe(pin^F)_2]\cdot 2CH_3CN$. Interestingly, the location of the global minimum is displaced to $\theta \sim 21°$ when the two pin^F ligands assume a $\delta\delta$ conformation, such as that observed experimentally for the two sites of **S′** and of $PPN[Li(MeOH)_4][Fe(pin^F)_2]$. Therefore, these calculations suggest that the geometry of the $[FeO_4]$ moiety is controlled, at least in part, by the intramolecular packing of the pin^F ligands, which appears to be more efficient for the $\delta\delta$ isomer. Thus, single-point calculations performed for geometry-optimized models of $\delta\lambda$- and $\delta\delta$-$[Fe(pin^F)_2]^{2-}$ predict that the $\delta\delta$ isomer is lower in energy. A similar behavior is obtained for the $[Zn(pin^F)_2]^{2-}$ analogues except that, in this case, the energy of the $\delta\delta$ isomer is only 18 cm^{-1}, ~0.05 kcal/mol, lower than that of the $\delta\lambda$. Most importantly, the potential energy curves obtained for $[Zn(pin^F)_2]^{2-}$ have only one minimum, each corresponding to a structure best described as quasi-tetrahedral. These theoretical structures are similar to those of the Zn(II) complexes structurally characterized to date. In particular, the $\delta\lambda$-$[Zn(pin^F)_2]^{2-}$ anion of $K_2[Zn(pin^F)_2]$ exhibits a $\theta = 88.4°$ and $\tau_4 = 0.80$, which are quite close to the $\theta = 88.7°$ and $\tau_4 = 0.82$ obtained for the $\delta\lambda$ theoretical structure. Since the Zn(II) ions have a d^{10} electronic configuration, their ligand field stabilization energies are null. Therefore, the geometries of these Zn(II) complexes are essentially determined by steric interactions. The dissimilarity of the potential energy curves obtained for the Zn(II) complexes and their Fe(II) analogues suggests that the stabilization of a planar $[FeO_4]$ moiety likely originates from an electronic effect.

Considering that at least one square-planar $[M(pin^F)_2]^{2-}$ species has been structurally characterized for each 3d M(II) ion with a d^6–d^9 configuration and that both $A_2[Zn(pin^F)_2]$ complexes reported to date enclose a quasi-tetrahedral geometry Zn(II) site, it is likely the population of the $3d_{xy}$ orbital plays the most important role in stabilizing a square planar geometry. Because this orbital points directly at the O atoms of the pin^F ligands, it has the highest energy among the 3d orbitals. Therefore, the $3d_{xy}$ orbital of $[M(pin^F)_2]^{2-}$ species becomes doubly occupied only for Zn(II) ions, which have a d^{10} electronic configuration. Inspection of Figure 11 shows that, as expected, the energy of the $|xy\rangle$ state is strongly affected by the planarity of the $[FeO_4]$ site such that at $\theta = 90°$, its CASSCF(5,6)-predicted value is only half of that obtained at $\theta = 0°$ (see next section for the details of the CASSCF calculations and a discussion of the electronic structures of **S**/**S′**). Furthermore, for $\tau_4 \leq 0.2$, there are one or more triplet states that have a lower energy than $|xy\rangle$. The mechanism through which the $|xy\rangle$ state promotes the planarity of the $[FeO_4]$ moiety is yet to be established.

3.4.3. Electronic Structure of Square-Planar Complexes ***S/S′***. We have investigated the electronic structure of the square-planar complexes **S** and **S′** by executing a series of DFT calculations using the BP86, B3LYP, and TPSSH functionals in conjunction with the 6-311G and def2-TZVPP basis sets. In addition, we have also performed *ab initio* CASSCF calculations using an active space spanned by six electrons, which populate the canonical 3d orbitals of the Fe(II) metal ion. These calculations used structural models derived not only from the experimental X-ray structures of **S**/**S′**, shown in Figure S20, but also from geometry optimizations performed using DFT. For these models, the $[Fe(pin^F)_2]^{2-}$ anion was oriented such that the *x*-axis bisected the two pin^F ligands and the *z*-axis was orthogonal to the $[FeO_4]$ plane (see Figure 12).

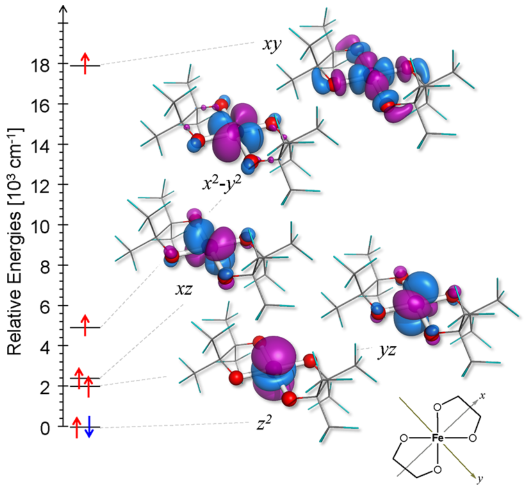

Figure 12. Crystal field splitting diagram inferred from a CASSCF(5,6)/def2-TZVPP calculation, which considered 5 quintet and 35 triplet states performed on a $[Fe(pin^F)_2]^{2-}$ anion, derived from the X-ray structure of **S**.

These computations have allowed us to infer the corresponding electronic ground-state configurations and provided us with theoretical estimates of the ZFS, ***g***, EFG, and ***A*** tensors. Subsequently, these results were compared with those obtained from simple crystal-field theory arguments.

Inspection of the DFT-predicted Fe orbital populations, presented in Tables S7, shows that, just as anticipated for square-planar compounds, the ground-state electronic configurations of **S**/**S′** are best described using the $|z^2\rangle$ =

$|(z^2)^2(yz)^1(xz)^1(xy)^1(x^2-y^2)^1|$ Slater determinant. This conclusion is further corroborated by our *ab initio* CASSCF calculations. Thus, the crystal field splitting diagram presented in Figures 12, derived from CASSCF(5,6) calculations that used a K$^+$-free structural model of the $[\mathrm{Fe(pin^F)_2}]^{2-}$ anion extracted from the experimental structure of **S**, highlights the CASSCF-predicted ground-state electronic configuration for which the single spin-down, β-electron occupies a $3d_{z^2}$ orbital. The analogous diagram derived for *site 2* of the X-ray structure of **S**′ is presented in Figure S21. These crystal field splitting patterns were inferred from the data presented in Table S8. The similarity of the predicted ground-state electronic configurations of **S** and **S**′ indicates that their respective Fe sites are only weakly perturbed by the corresponding $\{\mathrm{K(DME)_2}\}^+$ and $\{\mathrm{K(}C222)\}^+$ counterions. Additionally, the distortion of the two Fe sites of **S**′ away from planarity does not lead to a dramatic reorganization of their Fe site electronic configurations. For example, Figure S22, which summarizes the CASSCF(5,6)-predicted quintet states' energies, shows that the displacement of the two K$^+$ ions from the second coordination sphere of **S** leads to an increase of ∼400 cm^{-1} in the energy of the lowest excited orbital state $|yz\rangle$ (see first entries in columns 5 and 9 of the first section of Table S8). Therefore, the electrostatic interactions between the Fe(II) ion and the two K$^+$ cations located along the y-axis likely contribute to the stabilization of the $3d_{yz}$ orbital. Most importantly, the energy of the highest excited quintet state, $|xy\rangle$, is strongly influenced by the planarity of the [FeO$_4$] sites (see Figure 11). This conclusion is further corroborated by the energies of the $|xy\rangle$ state predicted for the two sites of **S**′, characterized by τ_4 = 0.27 and 0.37, which are ∼2600 and ∼4000 cm^{-1} lower than that predicted for **S** (τ_4 = 0.00) (see Figure S22).

The state energies predicted by our *ab initio* CASSCF(5,6) and CASSCF/NEVPT2(5,6) calculations lead to a crystal field splitting pattern such that presented in Figure 12 and Figure S21, namely, $\Delta_{yz} \lesssim \Delta_{xz} < \Delta_{x^2-y^2} \ll \Delta_{xy}$, where $\Delta_{\mathrm{ES}} = \varepsilon(\mathrm{GS} \rightarrow \mathrm{ES})$ is the energy of the excited state (ES) obtained by promoting a spin-down, β electron from the ground state (GS). However, analysis of the TD DFT-predicted single-electron excitations, summarized in Table S9, suggests that DFT predicts a much lower energy for the excited $|x^2-y^2\rangle$ state such that, typically, the crystal field splitting pattern inferred from these calculations is best described as $\Delta_{x^2-y^2} \lesssim \Delta_{xz} \lesssim \Delta_{yz} \ll \Delta_{xy}$. While we have not elucidated the origin of this discrepancy, critically, both CASSCF and DFT methods predict similar energies for the $\{|xz\rangle, |yz\rangle\}$ states. Changes in the magnitude of $\Delta_{x^2-y^2}$ have a minimal impact on the magnetic properties of **S**/**S**′, which can be traced to the fact that $\langle \mathrm{ES}|\hat{L}_z|z^2\rangle = 0$ and the only nonzero matrix elements involving the $|z^2\rangle$ ground state are $\langle z^2|\hat{\mathrm{L}}_x|yz\rangle = \langle xz|\hat{\mathrm{L}}_y|z^2\rangle = i\sqrt{3}$. Consequently, when only the quintet states are considered, the $|z^2\rangle$ ground state interacts through spin−orbit coupling with only $|xz\rangle$ and $|yz\rangle$ states but not with the excited $\{|x^2-y^2\rangle, |xy\rangle\}$. Therefore, using second-order perturbation theory, the quintet states' contribution to the ZFS parameters may be evaluated using eqs 5a and 5b.[45]

$$D = \lambda^2 \frac{3}{2}\left(\frac{1}{\Delta_{xz}} + \frac{1}{\Delta_{yz}}\right) \tag{5a}$$

$$E/D = \frac{\Delta_{xz} - \Delta_{yz}}{\Delta_{xz} + \Delta_{yz}} \tag{5b}$$

Assuming a spin−orbit coupling constant ∼20% lower than the free ion value, λ = −80 cm^{-1}, typically observed for iron(II) compounds, from these expressions and the experimental ZFS parameters of **S**, we obtain that Δ_{yz} = 1170 cm^{-1} and Δ_{xz} = 1380 cm^{-1}. Inspection of Tables S8 and S9 shows that these values are considerably lower than those derived from CASSCF(5,6) and TD DFT even when the typical error associated with these theoretical values are considered.[57] Thus, the TD DFT calculation performed at the BP86/def2-TZVPP level for the K$^+$ free $[\mathrm{Fe(pinF)_2}]^{2-}$ anion from the experimental structure of **S** predicts that Δ_{xz} = 6122 cm^{-1} and Δ_{yz} = 7739 cm^{-1}. At the same time, the CASSCF/NEVPT(5,6) run completed on the same model yielded Δ_{yz} = 2851 cm^{-1} and Δ_{xz} = 3250 cm^{-1}. This discrepancy may be traced to the fact that eqs 5a and 5b account for only the interactions with the excited quintet states ($D_{S=2}$). Thus, the experimental ZFS parameters also incorporate contributions from the spin−spin interaction (D_{SS}) and the excited triplet states ($D_{S=1}$), that is, $D = D_{S=2} + D_{S=1} + D_{\mathrm{SS}}$. While the former is expected to account for only a small correction, the latter may be quite large. In contrast to the ZFS tensor, the **g** tensor includes spin−orbit contributions from only the quintet states. Therefore, the perturbation theory expressions $\Delta g_x = -6\lambda/\Delta_{xz}$ and $\Delta g_y = -6\lambda/\Delta_{yz}$ provide an independent estimate of the two lowest excited-state energies such that, for λ = −80 cm^{-1}, we obtain Δ_{yz} = 2909 cm^{-1} and Δ_{xz} = 5274 cm^{-1}. Using these estimated energies to reassess the contribution of the S = 2 states, we find that $D_{S=2}$ = 5.12 cm^{-1} and $(E/D)_{S=2}$ = 0.29. These values, together with the DFT-predicted spin−spin contribution, $D_{\mathrm{SS}} \approx 0.45$ cm^{-1}, suggest that the contribution of the excited triplet states is dominant, that is, $D_{S=1} \sim 9.6$ cm^{-1}.

Theoretical estimates of ZFS and **g** tensors of **S** and **S**′ obtained from both CP DFT are summarized in Table S10, and *ab initio* CASSCF calculations including the NEVPT2 correction are compiled in Table S12. Just as observed experimentally for **S**, most of the CP DFT-predicted ZFS tensors have relatively small rhombicities, $E/D \leq 0.1$, and are characterized by positive D values. However, the magnitude of this parameter is roughly three times smaller than the experimental value observed for **S** and the corresponding *ab initio* values. This discrepancy may be traced to the higher excited-state energies predicted by DFT, just as inferred from the inspection of the corresponding TD DFT calculations of Table S9. Using the BP86/def2-TZVPP functional/basis set, for the isolated $[\mathrm{Fe(pin^F)_2}]^{2-}$, we obtained D = 4.92 cm^{-1} and E/D = 0.037. In contrast, when all five quintet and 35 triplet states are considered, the CASSCF(5,6) calculations yielded D = 14.89 cm^{-1} and E/D = 0.17. Despite the fact that these values compare quite well with those determined experimentally for **S**, most of the CASSCF(5,6) and CASSCF/NEVPT(5,6) calculations predict a much larger rhombicity, in some cases E/D as large as 1/3, which suggests that the sign of D is ambiguous. Indeed, inspection of Table S12 shows that some of these runs yielded negative D values. While in most cases the CP DFT calculations (see Table S11) predict that the contribution to the ZFS tensor of the quintet states is nearly as large as that of the triplet states, most of the CASSCF/NEVPT2(5,6) calculations suggest that $D_{S=1} \sim 5$ cm^{-1} (see Table S13).

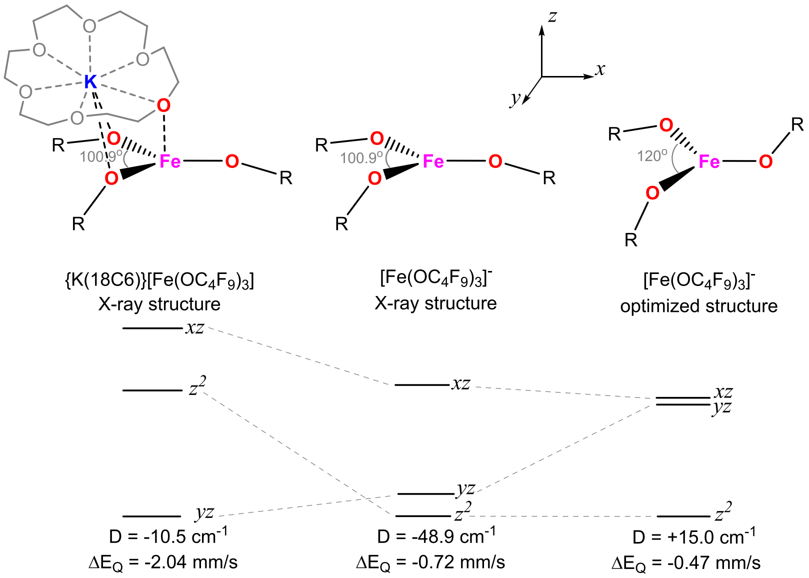

Figure 13. Crystal field splitting diagram of the lowest Fe(II) 3d orbitals and selected theoretical spectroscopic parameters derived from CASSCF(5,6) calculations performed for various structural models of **T**. Two structural models were derived from the experimental X-ray structure, and one was obtained from a geometry optimization performed at the BP86/def2-TZVPP level of theory; see text.

An unusual spectroscopic feature of all square-planar Fe(II) complexes characterized to date, including **S**/**S′**, is that they exhibit an unusually small quadrupole splitting (see Table 2). While the ΔE_Q of most high-spin ferrous compounds ranges from 1.5 to 3.4 mm/s, for **S**/**S′**, this value is much smaller; that is, only ~0.5 mm/s. This small value may be traced to the competition between the ligand and valence contributions to the EFG tensor. Interestingly, this behavior may be readily illustrated even with a very simple model consisting of four negative point charges arranged in a square around a central iron(II) ion. Thus, inspection of Table S14 shows that the EFG valence contribution generated by the single spin-down, β electron that populates the $3d_{z^2}$ orbital, which has a large negative component along z, is largely quenched by the ligands' contribution to EFG generated by the four ligands, which has a large positive component also along z. Inspection of Tables S15 and S16 shows that our DFT results clearly replicate these trends. Finally, the DFT-predicted isomer shift values, in particular those obtained for geometry-optimized models, are comparable with those observed experimentally, such that when using B3LYP/6-311G we obtained $\delta = 0.745$ mm/s for **S** (see Table S16).

As mentioned above, the ZFS tensor of **S** is dominated by the contribution of the triplet states. Therefore, to assess the magnitude of the Fermi contact component, $A_{FC} = -\kappa P$, of the hyperfine coupling tensor $\boldsymbol{A}$, we used the experimental Δg values and eq 6:

$$A_\xi = -P(\kappa + l_\xi + \Delta g_\xi) \qquad (6)$$

where $\xi = x, y, z$ and $\Delta g_\xi = g_\xi - g_e$. Additionally, $P = g_e\beta\langle r^{-3}\rangle_{3d}$ is a constant expressed in [Tesla], which depends on the radial extension of the Fe 3d orbitals and κ is a covalency reduction factor. The first term of eqs 6 and 8a−8c is the Fermi contact term, $A_{FC} = -P\kappa$, the second is the spin-dipolar contribution, $A_{SD,\xi} = -Pl_\xi$, and the last term for spin−orbit coupling, A_{SO}. In this case, owing to the $|z^2\rangle$ ground state of **S**, the l_ξ coefficients of the traceless dipolar contribution, $A_{SD} = -l_\xi P$, are $l_z = 1/7$ and $l_x = l_y = -1/14$.[48] Since we have three equations that relate six experimental quantities to two unknowns, we assessed P and κ by minimizing the difference between the theoretical and experimental A_ξ values. Using this procedure, we obtained $P = 43.2$ T and $\kappa = 0.55$, which leads to $A_{FC} \cong -23.8$ T. These values are fairly typical of four-coordinate, high-spin Fe(II) complexes with N/O/S coordination spheres. We have also obtained quantitative estimates of the $\boldsymbol{A}$ tensors from DFT calculations performed on models derived from the experimental and geometry-optimized structures (see Table S17). However, these values are strongly dependent on the basis set used and, in many cases, the predicted Fermi contact term is positive. Nevertheless, the magnitude of this term is much smaller than that observed experimentally. This behavior is consistent with other DFT investigations of hyperfine coupling tensors, which found that the experimental and theoretical values of the Fermi contact term often differ by a factor of ~1.8.[58]

3.4.4. Electronic Structure of T.

We have rationalized the spectroscopic behavior of **T** following a procedure broadly analogous to that used to investigate **S**/**S′** using structural models that include both the $[Fe(OC_4F_9)_3]^-$ complex anion and the $\{K(18C6)\}^+$ cation. Simple crystal field arguments suggest that an Fe(II) site with a trigonal planar geometry should exhibit a $|z^2\rangle$ ground state. Such a state was indeed observed for $[Ph_4P][Fe(SR)_3]\cdot 2MeCN\cdot C_7H_8$, shown in Scheme 1, which incorporates an $[FeS_3]$ site with an idealized C_{3h} point group symmetry.[25] However, our calculations predicted that **T** has an Fe ground-state electronic configuration best described using the $|yz\rangle = |(yz)^2(xz)^1(xy)^1(z^2)^1(x^2{-}y^2)^1|$ Slater determinant for which the $3d_{yz}$ orbital is doubly occupied (see Table S18). Moreover, the two lowest excited orbital states originate from the promotion of the spin-down, β electron to the $3d_{z^2}$ and $3d_{xz}$ orbitals. In this case, the z-axis was taken perpendicular to the plane of the $[FeO_3]$ site and the x-axis along the shortest Fe−O bond that is nearly parallel to the median of the smallest OFeO equatorial bond angle, which has a value of ~101° (see Figure 13). Importantly, our theoretical and computational analysis of the spectroscopic parameters detailed below clearly validate this electronic structure.

It is likely that the |*yz*⟩ ground state of **T** originates from the interaction of the $[Fe(OC_4F_9)_3]^-$ complex anion with the $\{K(18C6)\}^+$ cation. To explore the influence of this cation on the electronic structure of the Fe site, we have performed additional calculations on the isolated $[Fe(OC_4F_9)_3]^-$ anion using structural models derived from both the experimental structure and geometry optimizations. Some of these results are summarized in Figure 13. An unusual structural feature of $\{K(18C6)\}[Fe(OC_4F_9)_3]$ is that an oxygen atom belonging to the crown ether occupies the apical position of the Fe(II) site. Although the corresponding Fe−O bond length is ≥0.25 Å longer than the equatorial Fe−O bonds formed by the fluorinated alkoxo ligands, some of the DFT calculations predict for this interaction a bond order of ∼0.4 (see Table S19). Therefore, these calculations suggest that the Fe ion forms a weak coordinative bond with the cryptand, which destabilizes the $3d_{z^2}$ orbital and leads to a |*yz*⟩ ground state. As expected, in the absence of $\{K(18C6)\}^+$, we obtained a $|z^2\rangle$ ground state; see Tables S20 and S21. The CASSCF calculations performed for the experimental structure of the isolated complex anion indicate that the spin−orbit interaction within the $\{|yz\rangle, |z^2\rangle\}$ orbital quasi-doublet, formed by the ground state with a low-lying |*yz*⟩ excited state, would lead to an unquenching of the angular momentum along *x* and a large axial magnetic anisotropy, i.e., to a large, negative *D* value. Although the sum of the OFeO bond angles of the experimentally observed $[Fe(OC_4F_9)_3]^-$ complex anion is 359.1°, demonstrating a planar $[FeO_3]$ site, the individual OFeO angles are very different from one another ranging from 100.9 to 121.8 and 136.4° resulting in a $[FeO_3]$ core of approximate C_{2v} symmetry, represented in Figure 13, middle. Optimizing this structure leads to nearly equal OFeO angles and to a trigonal planar $[FeO_3]$ site with an approximate C_3 symmetry (see Figure 13, right). The CASSCF calculations performed for the geometry optimized models suggest that for this species, the spin−orbit coupling of the isolated $|z^2\rangle$ ground state to excited $\{|yz\rangle, |xz\rangle\}$ excited orbital quasi-doublet would lead to a ZFS characterized by a positive *D* value, similar to that observed for $[Ph_4P][Fe(SR)_3]\cdot 2MeCN\cdot C_7H_8$. Therefore, these calculations suggest that the asymmetry of the planar $[FeO_3]$ site of **T**, in particular the low ∼101° O−Fe−O bond angle, may be traced to the interaction of the corresponding fluorinated *t*-butoxide ligands with the K^+ ion. Moreover, inspection of Table S22 reveals that, for the isolated complex anion, we obtained a quadrupole splitting, $\Delta E_Q = 1.40$ mm/s, which, just like that of **S** and other square- and trigonal-planar complexes, is unusually low for high-spin Fe(II) sites (see Table 2). This low value originates from the competition between the valence contribution of the $|z^2\rangle$ state and that of the ligands which have opposite signs and the largest components perpendicular to the molecular plane. In contrast, the theoretical ΔE_Q values obtained for $\{K(18C6)\}[Fe(OC_4F_9)_3]$ are rather large, typical of high-spin Fe(II) sites, in concordance with the experimental value. Moreover, the valence and ligand contributions to the EFG tensor of this compound, shown also in Table S22, combine in such a fashion that they lead to a large EFG asymmetry parameter, $\eta \gtrsim 0.8$, *vide infra*.

Both our CP DFT and *ab initio* CASSCF calculations reproduce the experimental zero-field Mössbauer parameters of **T** reasonably well (see Table S23). For example, while BP86/def2-TZVPP yields $\Delta E_{Q,th} = -2.01$ mm/s and $\eta_{th} = 0.87$, CASSCF(5,6) predicts $\Delta E_{Q,th} = -2.04$ mm/s and $\eta_{th} = 0.87$. These theoretical ΔE_Q values compare well with the experimental quantity particularly when considering the ∼1.0 mm/s error often encountered while computing quadrupole splitting values.[58,48] The large asymmetry parameters of the experimental and theoretical EFG tensors, $\eta = 0.8{-}0.9$, suggest that the sign of ΔE_Q is not well-defined. Indeed, inspection of Table S23 shows that while the ΔE_Q values derived using 6-311G are positive, those obtained using the def2-TZVPP and TZVP basis sets are negative. Moreover, inspection of Table S23 shows that although the theoretical isomer shift values obtained at different levels of theory are ∼0.2 mm/s smaller than the experimental quantity, these theoretical values are still considerably larger than those of most trigonal Fe(II) species for which $\delta = 0.48{-}0.8$ mm/s.[59,60] We note that these values were obtained for the experimental structure, not for geometry-optimized models, which might explain the larger than expected error of ∼0.1 mm/s. Since for an isolated |*yz*⟩ orbital state we anticipate a positive ΔE_Q and an axial EFG tensor (that is, $\eta = 0$), we sought to understand the origin of the large η value.

To rationalize the experimental EFG tensor of **T**, we first considered a very crude model consisting of an Fe(II) ion with a ground state for which the $3d_{yz}$ orbital is doubly occupied, surrounded by four negative point charges situated at the corners of a trigonal pyramid (see Figure S23). For this model, the three equatorial charges lead to a large positive EFG component along *z*, which is counterbalanced by a negative component along the same axis generated by the apical ligand. Together, the four charges yield a relatively modest EFG tensor, which has its largest negative component along *z* (see Table S24). Adding this contribution to the valence component of the doubly occupied $3d_{yz}$ orbital, for which the largest positive component is found along *x*, leads to a highly asymmetric total EFG tensor with its smallest contribution along *x*. In the next step, we have obtained a more quantitative estimate of ligands' contributions for both the isolated $[Fe(OC_4F_9)_3]^-$ anion and unabridged $\{K(18C6)\}[Fe(OC_4F_9)_3]$ by replacing the Fe(II) ions with Zn(II), which have a d^{10} electronic configuration and therefore a null valence contribution. Inspection of Table S22 shows that our DFT calculations reproduce many of the patterns inferred from the much simpler point charge model except that the smallest component of the total EFG tensor is found along *y*. Therefore, this analysis suggests that the interaction of the Fe site with the cryptand ligand not only stabilizes a |*yz*⟩ ground state but also leads to a highly asymmetric EFG tensor and a large η value.

In order to rationalize the magnetic properties of **T**, we have obtained estimates of the d−d excitation energies as well as of the theoretical ZFS, ***g***, and ***A*** tensors from TD and CP DFT and from CASSCF/NEVPT2 calculations performed for the unabridged crystal structure of $\{K(18C6)\}[Fe(OC_4F_9)_3]$. Moreover, we have compared these quantities, listed in Tables S25 and S26, with those obtained from treating the spin−orbit coupling, $\hat{H}_{SO} = \lambda\hat{\mathbf{L}}\cdot\hat{\mathbf{S}}$, as a perturbation up to the second order of the crystal field interaction where the splitting of Fe 3d orbitals was inferred from the TD DFT and CASSCF calculations. Inspection of Table S25, derived from TD DFT calculations, as well as of Figure 14 and Tables S25−S27, derived from CASSCF/NEVPT2 calculations, shows a similar order of d−d excitation energies, which leads to a crystal field

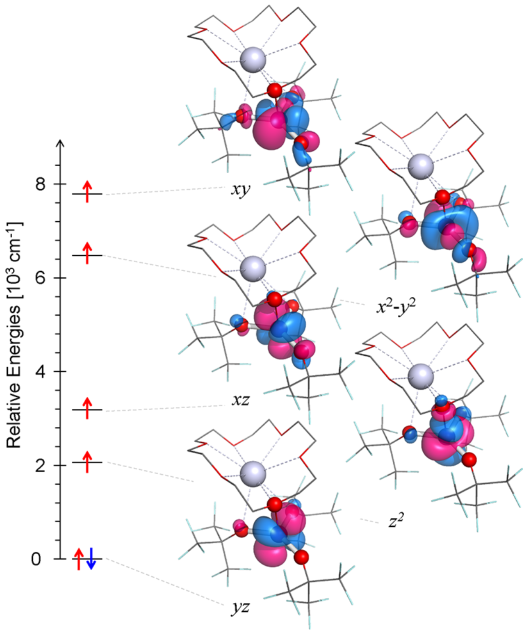

Figure 14. Crystal field splitting diagram inferred from a CASSCF(5,6)/def2-TZVPP calculation, which considered 5 quintet and 35 triplet states performed on the unabridged X-ray structure of **T**.

splitting pattern such that $\Delta_{z^2} \lesssim \Delta_{xz} \ll \Delta_{x^2-y^2} \lesssim \Delta_{xy}$. The most important difference between the DFT and CASSCF calculations is that the energies of the two lowest quintet states derived from TD DFT are twice as large as those obtained from CASSCF(5,6) and CASSCF/NEVPT2(5,6) calculations. Since these states have the strongest influence on the ZFS of **T**, this difference leads to CP DFT-predicted D values, which are approximatively three times smaller than those derived from CASSCF (see Tables S28 and S29). For example, while BP86/def2-TZVPP yielded $D = -2.67$ cm^{-1}, the CASSCF/NEVPT2(5,6) calculations, which considered all five quintet states and 10 triplets, provided $D = -9.057$ cm^{-1} and $E/D = 0.24$. We note that the latter theoretical values are in excellent agreement with those derived from the HFEPR studies of **T**. Although both methods predict that the contribution of the excited triplet states ($\alpha \rightarrow \beta$ transitions) to the ZFS amounts to $D_{S=1} \sim -1$ cm^{-1}, the CP DFT results indicate that this contribution is nearly equal to that of the quintet states. Furthermore, these calculations also suggested that the spin−spin contribution to the ZFS is relatively small, that is, $D_{SS} \sim -0.5$ cm^{-1}. In contrast, the CASSCF and our crystal-field model suggest that the contribution of the quintet states to the ZFS of **T**, of the $\beta \rightarrow \beta$ excitations, is dominant as shown in Table S30.

An interesting feature of the spin−orbit interaction in this system is that although the $|z^2\rangle$ and $|xz\rangle$ states have comparable energies, we observe a ZFS tensor characterized by a negative D and a large rhombicity. This observation may be traced to the larger magnitude of the $\langle z^2|\hat{L}_x|yz\rangle = i\sqrt{3}$ matrix element when compared to that of $\langle xz|\hat{L}_z|yz\rangle = -i$. Due to their higher energies, the $|xy\rangle$, $|x^2-y^2\rangle$ states and the corresponding matrix elements, $\langle xy|\hat{L}_y|yz\rangle = \langle x^2-y^2|\hat{L}_x|yz\rangle = i$, do not play an important role in this case. Therefore, we find that the ZFS is quantized along the x-molecular axis such that the z-axis of the spin Hamiltonian of eq 1 is essentially parallel to the shortest FeO bond (see Table S31).

When the contributions of the triplets and of the higher energy $|xy\rangle$ and $|x^2-y^2\rangle$ quintet states are ignored, we obtained the following expressions for the ZFS parameters:

$$D = -\lambda^2\left(\frac{3}{\Delta_{z^2}} + \frac{1}{2\Delta_{xz}}\right) \tag{7a}$$

$$E/D = \frac{2\Delta_{z^2}}{\Delta_{z^2} - 6\Delta_{xz}} \tag{7b}$$

where λ is the spin−orbit coupling constant. Assuming that $\Delta_{z^2} = 2000$ cm^{-1}, $\Delta_{xz} = 3000$ cm^{-1}, values similar to those derived from the CASSCF calculations, and $\lambda = -80$ cm^{-1}, which is a covalently reduced value often observed for low-coordinate Fe(II) ions, we predict that $D = -10.6$ cm^{-1} and $|E/D| = 0.25$. Analogously, for the $\boldsymbol{g}$ tensor component aligned with the x-molecular axis, we find $\Delta g_z = -6\lambda/\Delta_{z^2} = 0.24$. Notwithstanding the coarseness of this model, we find that these theoretical values are in excellent agreement with the experimental data. We note that, due to the difficulties we experienced in obtaining accurate experimental estimates of $\{g_x, g_y\}$ from the current HFEPR data recorded for **T**, these parameters were excluded from our analysis.

Using the same model to evaluate the components of the hyperfine coupling tensor $\boldsymbol{A}$, we derive the following expressions:

$$A_x = -P\left(\kappa + l_x + \frac{6\lambda}{\Delta_{z^2}}\right) \tag{8a}$$

$$A_y = -P(\kappa + l_y) \tag{8b}$$

$$A_z = -P\left(\kappa + l_z + \frac{2\lambda}{\Delta_{xz}}\right) \tag{8c}$$

For a $|yz\rangle$ ground state, such as that inferred for **T**, the l_ξ coefficients of the traceless A_{SD} tensor are $l_x = -1/7$ and $l_y = l_z = 1/14$. By setting $A_x = -3.6$ T and $A_z = -18.5$T and solving for P and κ, we obtain $P = 37.16$T and $\kappa = 0.48$ such that $A_{FC} = -17.83$T. Although these values are lower than those of typical four-coordinate complexes, including **S**, they are comparable to those determined for $[Ph_4P][Fe(SR)_3]\cdot 2MeCN\cdot C_7H_8$, namely, $P = 38.71$T and $A_{FC} = 15.87$ T.[25] Although these values lead to $A_y = -20.5$T, which is smaller than the corresponding -24.5 T experimental value, given the shortcomings of this model and the difficulty of determining this quantity experimentally, we consider this solution to be satisfactory. More rigorous, quantitative estimates of the various tensor components were obtained from CP DFT calculations performed on the unabridged experimental structure of **T**. However, inspection of Table S32 shows that even though they have a similar magnitude as those obtained from the 6-311G basis set, the A_{FC} and A_{SD} values obtained from the calculations that employed def2-TZVPP have the wrong sign. Nevertheless, the agreement between the DFT-derived A_{FC} and A_{SD} values and those obtained from the simple crystal field model presented above is reasonable, particularly when the difficulty of obtaining accurate A_{FC} using DFT is considered.[58] As expected, due to the higher transition energies, these DFT calculations underestimate the spin−orbit contribution to the $\boldsymbol{A}$ tensor. The perturbation theory expressions of the ZFS, $\boldsymbol{g}$, and $\boldsymbol{A}$ tensor components that include the contributions of the higher energy $|xy\rangle$ and $|x^2-y^2\rangle$ quintet states are included in the SI (see Equations S1−S3). Using these expressions, instead of eqs 7a and 7b and eqs 8a, 8b, and 8c, to rationalize the spectroscopic properties of **T** did not lead to an improved agreement with the experimental data.

4. CONCLUSIONS

In conclusion, we have presented a novel complex, $\{K(C222)\}_2[Fe(pin^F)_2]$, **S′**, and have compared its electronic structure to the analogous and previously published $\{K(DME)_2\}_2[Fe(pin^F)_2]$, **S**. We additionally investigated previously published complex **T**, $\{K(18C6)\}[Fe(OC_4F_9)_3]$. These high-spin, planar complexes were further compared to known literature complexes with O-donor ligand environments and their electronic structures previously studied in detail by ^{57}Fe Mössbauer spectroscopy: 4-coordinate $(CF_3ONO)FeCl$, $[Li_2(THF)_4Fe(O(SiPh_2O)_2)_2]$ and the α-Fe active site of Mordenite, as well as 3-coordinate $[Na(DME)Fe(OSiPh_3)_3]$, $[Fe(SR)_3]^-$, and $Li(THF)_2Fe(SR)_3$. Importantly, the structure of the α-Fe site of iron-doped mordenite was inferred not from crystallographic studies but rather from spectroscopic investigations, using Mössbauer and magnetic circular dichroism spectroscopies (the latter was not used here). Such an approach is more commonly used in bioinorganic chemistry. Therefore, our study not only furthers our understanding of these unusual sites but also allows us to gauge the extent to which these sites may be distorted away from a square planar geometry but still retain their unusual spectroscopic features. Thus, we have completed a detailed spectroscopic and theoretical trigonal of trigonal, **T**, and the two square planar, **S** and **S′**, high-spin Fe(II) complexes. The distorted trigonal geometry, unanticipated $|yz\rangle$ ground state, and negative axial ZFS parameter D of **T** may be explained by considering the interaction between its Fe site and countercation. In contrast, the countercations of **S**/**S′** have a minimal influence on the electronic structure of their Fe sites. Instead, the distortion of the Fe sites of **S′** may be traced, in part, to the conformations of the supporting pin^F ligands. Nevertheless, both compounds incorporate Fe sites with a $|z^2\rangle$ ground state, which leads to a positive D value and unusually small ΔE_Q. **T**, **S**, and **S′** are therefore examples of a small subset of unusually high-spin, planar Fe(II) compounds, resembling the active sites of iron-doped zeolites including Mordenite.

ASSOCIATED CONTENT

Supporting Information

The Supporting Information is available free of charge at https://pubs.acs.org/doi/10.1021/acs.inorgchem.3c03236.

> Additional HFEPR and Mössbauer data, theoretical simulations, analytical expressions of second-order crystal field theory expressions of spectroscopic parameters, summary of computational results, geometry-optimized structures as well as synthetic procedures and characterizations of **1**−**5**, and crystallographic data collection and refinement parameters (PDF)

Accession Codes

CCDC 2221534 contains the supplementary crystallographic data for this paper. These data can be obtained free of charge via www.ccdc.cam.ac.uk/data_request/cif, or by emailing data_request@ccdc.cam.ac.uk, or by contacting The Cambridge Crystallographic Data Centre, 12 Union Road, Cambridge CB2 1EZ, UK; fax: +44 1223 336033.

AUTHOR INFORMATION

Corresponding Authors

Linda H. Doerrer − *Department of Chemistry, Boston University, Boston, Massachusetts 02215, United States;* orcid.org/0000-0002-2437-6374; Email: doerrrer@bu.edu

Sebastian A. Stoian − *Department of Chemistry, University of Idaho, Moscow, Idaho 83844, United States;* orcid.org/0000-0003-3362-7697; Email: sstoian@uidaho.edu

Authors

Léa A. Toubiana − *Department of Chemistry, Boston University, Boston, Massachusetts 02215, United States;* orcid.org/0000-0003-0050-5845

Adam Valaydon-Pillay − *Department of Chemistry, University of Idaho, Moscow, Idaho 83844, United States*

Jessica K. Elinburg − *Department of Chemistry, Boston University, Boston, Massachusetts 02215, United States;* orcid.org/0000-0003-3064-3771

Jeffrey W. Bacon − *Department of Chemistry, Boston University, Boston, Massachusetts 02215, United States*

Andrew Ozarowski − *National High Magnetic Field Laboratory, Florida State University, Tallahassee, Florida 32310, United States;* orcid.org/0000-0001-6225-9796

Complete contact information is available at: https://pubs.acs.org/10.1021/acs.inorgchem.3c03236

Author Contributions

$^{\#}$L.A.T. and A.V.-P. have contributed equally to this work.

Notes

The authors declare no competing financial interest.

ACKNOWLEDGMENTS

Acknowledgement is made to the donors of the American Chemical Society Petroleum Research Fund for support of this research through a DNI grant (62278-DNI3) to S.A.S. L.H.D. and L.A.T. thank the National Science Foundation (NSF) for support of this work (CHE 2102532 to L.H.D.), and the National Institutes of Health (S10OD028585 to Boston University for SCXR diffractometer). *A portion of this work was performed at the National High Magnetic Field Laboratory, which is supported by National Science Foundation Cooperative Agreement No. DMR-2128556 and the State of Florida.* Boston University stands on the territory of the Wampanoag and the Massachusett People. The National High Magnetic Field Laboratory is located on the ancestral homelands of the Seminole Tribe. The University of Idaho, Moscow, is located on the homelands of the Nimiipuu (Nez Perce), Palus (Palouse) and Schitsu'umsh (Coeur d'Alene) tribes. We extend gratitude to the indigenous people that have called these places home, since time immemorial.

REFERENCES

(1) *Spin States in Biochemistry and Inorganic Chemistry: Influence on Structure and Reactivity*; Swart, M.; Salgueiro, M. C., Eds.; Wiley: Chichester, West Sussex, United Kingdom, 2016.

(2) Collins, T. J.; Ryabov, A. D. Targeting of High-Valent Iron-TAML Activators at Hydrocarbons and Beyond. *Chem. Rev.* **2017**, *117* (13), 9140−9162.

(3) Marks, T. *Methane to Methanol What's Known and Questions/Challenges*. 18.

(4) Neidig, M. L.; Solomon, E. I. Structure−Function Correlations in Oxygen Activating Non-Heme Iron Enzymes. *Chem. Commun.* **2005**, *47*, 5843.

(5) Solomon, E. I.; Brunold, T. C.; Davis, M. I.; Kemsley, J. N.; Lee, S.-K.; Lehnert, N.; Neese, F.; Skulan, A. J.; Yang, Y.-S.; Zhou, J. Geometric and Electronic Structure/Function Correlations in Non-Heme Iron Enzymes. *Chem. Rev.* **2000**, *100* (1), 235−350.

(6) Price, J. C.; Barr, E. W.; Tirupati, B.; Bollinger, J. M.; Krebs, C. The First Direct Characterization of a High-Valent Iron Intermediate in the Reaction of an α-Ketoglutarate-Dependent Dioxygenase: A High-Spin Fe(IV) Complex in Taurine/α-Ketoglutarate Dioxygenase (TauD) from *Escherichia Coli*. *Biochemistry* **2003**, *42* (24), 7497−7508.

(7) Rohde, J.-U.; In, J.-H.; Lim, M. H.; Brennessel, W. W.; Bukowski, M. R.; Stubna, A.; Münck, E.; Nam, W., Jr.; Que, L. Crystallographic and Spectroscopic Characterization of a Nonheme Fe(IV)═O Complex. *Science* **2003**, *299* (5609), 1037−1039.

(8) Seo, M. S.; In, J.-H.; Kim, S. O.; Oh, N. Y.; Hong, J.; Kim, J.; Que, L.; Nam, W. Direct Evidence for Oxygen-Atom Exchange between Nonheme Oxoiron(IV) Complexes and Isotopically Labeled Water. *Angew. Chem., Int. Ed.* **2004**, *43* (18), 2417−2420.

(9) Snyder, B. E. R.; Bols, M. L.; Schoonheydt, R. A.; Sels, B. F.; Solomon, E. I. Iron and Copper Active Sites in Zeolites and Their Correlation to Metalloenzymes. *Chem. Rev.* **2018**, *118* (5), 2718−2768.

(10) Snyder, B. E. R.; Vanelderen, P.; Bols, M. L.; Hallaert, S. D.; Böttger, L. H.; Ungur, L.; Pierloot, K.; Schoonheydt, R. A.; Sels, B. F.; Solomon, E. I. The Active Site of Low-Temperature Methane Hydroxylation in Iron-Containing Zeolites. *Nature* **2016**, *536* (7616), 317−321.

(11) Chambers, M. B.; Groysman, S.; Villagrán, D.; Nocera, D. G. Iron in a Trigonal Tris(Alkoxide) Ligand Environment. *Inorg. Chem.* **2013**, *52* (6), 3159−3169.

(12) Yelin, S.; Limberg, C. Molecular Structural Motifs and O$_2$ Activation Inspired by Enzymes and Solid Catalysts. *Catal. Lett.* **2020**, *150* (1), 1−11.

(13) Cantalupo, S. A.; Fiedler, S. R.; Shores, M. P.; Rheingold, A. L.; Doerrer, L. H. High-Spin Square-Planar Co^{II} and FeII Complexes and Reasons for Their Electronic Structure. *Angew. Chem., Int. Ed.* **2012**, *51* (4), 1000−1005.

(14) Tahsini, L.; Specht, S. E.; Lum, J. S.; Nelson, J. J. M.; Long, A. F.; Golen, J. A.; Rheingold, A. L.; Doerrer, L. H. Structural and Electronic Properties of Old and New A $_2$ [M(Pin^F)$_2$] Complexes. *Inorg. Chem.* **2013**, *52* (24), 14050−14063.

(15) Cantalupo, S. A.; Lum, J. S.; Buzzeo, M. C.; Moore, C.; DiPasquale, A. G.; Rheingold, A. L.; Doerrer, L. H. Three-Coordinate Late Transition Metal Fluorinated Alkoxide Complexes. *Dalton Trans.* **2010**, *39* (2), 374−383.

(16) Wurzenberger, X.; Piotrowski, H.; Klüfers, P. A Stable Molecular Entity Derived from Rare Iron(II) Minerals: The Square-Planar High-Spin-d^6 Fe^{II}O$_4$ Chromophore. *Angew. Chem., Int. Ed.* **2011**, *50* (21), 4974−4978.

(17) Wurzenberger, X.; Neumann, C.; Klüfers, P. Enticing Cobalt into Planarity: Can a Pair of Diolato Ligands Make It Happen? *Angew. Chem., Int. Ed.* **2013**, *52* (19), 5159−5161.

(18) Pascualini, M. E.; Di Russo, N. V.; Thuijs, A. E.; Ozarowski, A.; Stoian, S. A.; Abboud, K. A.; Christou, G.; Veige, A. S. A High-Spin Square-Planar Fe(II) Complex Stabilized by a trianionic Pincer-Type Ligand and Conclusive Evidence for Retention of Geometry and Spin State in Solution. *Chem. Sci.* **2015**, *6* (1), 608−612.

(19) Pascualini, M. E.; Stoian, S. A.; Ozarowski, A.; Abboud, K. A.; Veige, A. S. Solid State Collapse of a High-Spin Square-Planar Fe(II) Complex, Solution Phase Dynamics, and Electronic Structure Characterization of an Fe$^{(II)}{}_2$ Dimer. *Inorg. Chem.* **2016**, *55* (11), 5191−5200.

(20) Pinkert, D.; Demeshko, S.; Schax, F.; Braun, B.; Meyer, F.; Limberg, C. A Dinuclear Molecular Iron(II) Silicate with Two High-Spin Square-Planar FeO $_4$ Units. *Angew. Chem., Int. Ed.* **2013**, *52* (19), 5155−5158.

(21) Manicke, N.; Hoof, S.; Keck, M.; Braun-Cula, B.; Feist, M.; Limberg, C. A Hexanuclear Iron(II) Layer with Two Square-Planar FeO$_4$ Units Spanned by Tetrasiloxide Ligands: Mimicking of Minerals and Catalysts. *Inorg. Chem.* **2017**, *56* (14), 8554−8561.

(22) Pinkert, D.; Keck, M.; Tabrizi, S. G.; Herwig, C.; Beckmann, F.; Braun-Cula, B.; Kaupp, M.; Limberg, C. A High-Spin Square Planar Iron(II)-Siloxide and Its Tetrahedral Allogon − Structural and Spectroscopic Models of Fe-Zeolite Sites. *Chem. Commun.* **2017**, *53* (57), 8081−8084.

(23) Pascualini, M. E.; Stoian, S. A.; Ozarowski, A.; Di Russo, N. V.; Thuijs, A. E.; Abboud, K. A.; Christou, G.; Veige, A. S. Synthesis and Characterization of a Family of M^{2+} Complexes Supported by a trianionic ONO^{3-} Pincer-Type Ligand: Towards the Stabilization of High-Spin Square-Planar Complexes. *Dalton Trans.* **2015**, *44* (46), 20207−20215.

(24) MacDonnell, F. M.; Ruhlandt-Senge, K.; Ellison, J. J.; Holm, R. H.; Power, P. P. Sterically Encumbered Iron(II) Thiolate Complexes: Synthesis and Structure of Trigonal Planar [Fe(SR)$_3$]$^-$ (R = 2,4,6-t-Bu$_3$C$_6$H$_2$) and Mössbauer Spectra of Two- and Three-Coordinate Complexes. *Inorg. Chem.* **1995**, *34* (7), 1815−1822.

(25) Sanakis, Y.; Power, P. P.; Stubna, A.; Münck, E. Mössbauer Study of the Three-Coordinate Planar Fe^{II} Thiolate Complex [Fe(SR)$_3$]$^-$ (R = C$_6$H$_2$ −2,4,6-tBu$_3$): Model for the Trigonal Iron Sites of the MoFe$_7$S$_9$:Homocitrate Cofactor of Nitrogenase. *Inorg. Chem.* **2002**, *41* (10), 2690−2696.

(26) Holland, P. L. Distinctive Reaction Pathways at Base Metals in High-Spin Organometallic Catalysts. *Acc. Chem. Res.* **2015**, *48* (6), 1696−1702.

(27) Evans, D. F. 400. The Determination of the Paramagnetic Susceptibility of Substances in Solution by Nuclear Magnetic Resonance. *J. Chem. Soc.* **1959**, 2003.

(28) Hassan, A. K.; Pardi, L. A.; Krzystek, J.; Sienkiewicz, A.; Goy, P.; Rohrer, M.; Brunel, L.-C. Ultrawide Band Multifrequency High-Field EMR Technique: A Methodology for Increasing Spectroscopic Information. *J. Magn. Reson.* **2000**, *142* (2), 300−312.

(29) Telser, J.; Krzystek, J.; Ozarowski, A. High-Frequency and High-Field Electron Paramagnetic Resonance (HFEPR): A New Spectroscopic Tool for bioinorganic Chemistry. *J. Biol. Inorg. Chem.* **2014**, *19* (3), 297−318.

(30) Neese, F. The ORCA Program System: The ORCA Program System. *WIREs Comput. Mol. Sci.* **2012**, *2* (1), 73−78.

(31) Neese, F. Software Update: The ORCA Program System—Version 5.0. *WIREs Comput. Mol. Sci.* **2022**, *12* (5), No. e1606.

(32) Lee, C.; Yang, W.; Parr, R. G. Development of the Colle-Salvetti Correlation-Energy Formula into a Functional of the Electron Density. *Phys. Rev. B* **1988**, *37* (2), 785−789.

(33) Becke, A. D. Density-Functional Exchange-Energy Approximation with Correct Asymptotic Behavior. *Phys. Rev. A* **1988**, *38* (6), 3098−3100.

(34) Perdew, J. P.; Kurth, S.; Zupan, A.; Blaha, P. Accurate Density Functional with Correct Formal Properties: A Step Beyond the Generalized Gradient Approximation. *Phys. Rev. Lett.* **1999**, *82* (12), 2544−2547.

(35) Krishnan, R.; Binkley, J. S.; Seeger, R.; Pople, J. A. Self-consistent Molecular Orbital Methods. XX. A Basis Set for Correlated Wave Functions. *J. Chem. Phys.* **1980**, *72* (1), 650−654.

(36) Weigend, F.; Ahlrichs, R. Balanced Basis Sets of Split Valence, Triple Zeta Valence and Quadruple Zeta Valence Quality for H to Rn: Design and Assessment of Accuracy. *Phys. Chem. Chem. Phys.* **2005**, *7* (18), 3297.

(37) Neese, F. An Improvement of the Resolution of the Identity Approximation for the Formation of the Coulomb Matrix. *J. Comput. Chem.* **2003**, *24* (14), 1740−1747.

(38) Neese, F.; Wennmohs, F.; Hansen, A.; Becker, U. Efficient, Approximate and Parallel Hartree−Fock and Hybrid DFT Calculations. A 'Chain-of-Spheres' Algorithm for the Hartree−Fock Exchange. *Chem. Phys.* **2009**, *356* (1−3), 98−109.

(39) Stoychev, G. L.; Auer, A. A.; Neese, F. Automatic Generation of Auxiliary Basis Sets. *J. Chem. Theory Comput.* **2017**, *13* (2), 554−562.

(40) Angeli, C.; Cimiraglia, R.; Evangelisti, S.; Leininger, T.; Malrieu, J.-P. Introduction of n -Electron Valence States for Multireference Perturbation Theory. *J. Chem. Phys.* **2001**, *114* (23), 10252−10264.

(41) Neese, F. Prediction and Interpretation of the 57Fe Isomer Shift in Mössbauer Spectra by Density Functional Theory. *Inorg. Chim. Acta* **2002**, *337*, 181−192.

(42) Römelt, M.; Ye, S.; Neese, F. Calibration of Modern Density Functional Theory Methods for the Prediction of ^{57}Fe Mössbauer Isomer Shifts: Meta-GGA and Double-Hybrid functionals. *Inorg. Chem.* **2009**, *48* (3), 784−785.

(43) Vrajmasu, V.; Münck, E.; Bominaar, E. L. Density Functional Study of the Electric Hyperfine Interactions and the Redox-Structural Correlations in the Cofactor of nitrogenase. Analysis of General Trends in ^{57}Fe Isomer Shifts. *Inorg. Chem.* **2003**, *42* (19), 5974−5988.

(44) Vrajmasu, V. V.; Bominaar, E. L.; Meyer, J.; Münck, E. Mössbauer Study of Reduced Rubredoxin As Purified and in Whole Cells. Structural Correlation Analysis of Spin Hamiltonian Parameters. *Inorg. Chem.* **2002**, *41* (24), 6358−6371.

(45) Abragam, A.; Bleaney, B.*Electron Paramagnetic Resonance of Transition Ions*; Dover Publications, Inc.: Mineola NY, 1986. Eqs 7.26 and 7.71.

(46) Krzystek, J.; Zvyagin, S. A.; Ozarowski, A.; Trofimenko, S.; Telser, J. Tunable-Frequency High-Field Electron Paramagnetic Resonance. *J. Magn. Reson.* **2006**, *178* (2), 174−183.

(47) Hendrich, M. P.; Debrunner, P. G. Integer-Spin Electron Paramagnetic Resonance of Iron Proteins. *Biophys. J.* **1989**, *56* (3), 489−506.

(48) Gütlich, P.; Bill, E.; Trautwein, A. X. *Mössbauer Spectroscopy and Transition Metal Chemistry: Fundamentals and Application*; Springer: Berlin, Heidelberg, 2011.

(49) Yelin, S.; Cula, B.; Limberg, C. Low-Coordinated Iron(II) Siloxide Complexes − Structural Diversity and Reactivity Towards O_2 and Oxygen Atom Transfer Reagents. *Eur. J. Inorg. Chem.* **2022**, *2022* (14), No. e202200078.

(50) Bakac, A.; Martinho, M.; Münck, E. ^{57}Fe Mössbauer Spectroscopy in Chemistry and Biology. In *Physical inorganic chemistry principles, methods, and models*; John Wiley & Sons, Inc. 2010.

(51) Que, Jr, L. *Physical Methods in bioinorganic Chemistry: Spectroscopy and Magnetism*; University Science Books, 2000.

(52) Schilter, D.; Nilges, M. J.; Chakrabarti, M.; Lindahl, P. A.; Rauchfuss, T. B.; Stein, M. Mixed-Valence Nickel−Iron Dithiolate Models of the [NiFe]-Hydrogenase Active Site. *Inorg. Chem.* **2012**, *51* (4), 2338−2348.

(53) Stoian, S. A.; Moshari, M.; Ferentinos, E.; Grigoropoulos, A.; Krzystek, J.; Telser, J.; Kyritsis, P. Electronic Structure of Tetrahedral, $S = 2$, $[\mathrm{Fe}\{(\mathrm{EP}^i\mathrm{Pr}_2)_2\mathrm{N}\}_2]$, E = S, Se, Complexes: Investigation by High-Frequency and -Field Electron Paramagnetic Resonance, ^{57}Fe Mössbauer Spectroscopy, and Quantum Chemical Studies. *Inorg. Chem.* **2021**, *60*, 10990.

(54) Zimmermann, R.; Spiering, H.; Ritter, G. Mössbauer Spectra of the Tetrakis-(1,8-Naphthyridine) Iron(II)Perchlorate in External Magnetic Fields. Evidence of Slow Relaxation in Paramagnetic Iron(II). *Chem. Phys.* **1974**, *4* (1), 133−141.

(55) Stoian, S. A.; Smith, J. M.; Holland, P. L.; Münck, E.; Bominaar, E. L. Mössbauer, Electron Paramagnetic Resonance, and Theoretical Study of a High-Spin, Four-Coordinate Fe(II) Diketiminate Complex. *Inorg. Chem.* **2008**, *47* (19), 8687−8695.

(56) Yang, L.; Powell, D. R.; Houser, R. P. Structural Variation in Copper(I) Complexes with Pyridylmethylamide Ligands: Structural Analysis with a New Four-Coordinate Geometry Index, τ_4. *Dalton Trans.* **2007**, *9*, 955−964.

(57) Wiberg, K. B.; Stratmann, R. E.; Frisch, M. J. A Time-Dependent Density Functional Theory Study of the Electronically Excited States of Formaldehyde, Acetaldehyde and Acetone. *Chem. Phys. Lett.* **1998**, *297* (1−2), 60−64.

(58) Sinnecker, S.; Slep, L. D.; Bill, E.; Neese, F. Performance of Nonrelativistic and Quasi-Relativistic Hybrid DFT for the Prediction of Electric and Magnetic Hyperfine Parameters in ^{57}Fe Mössbauer Spectra. *Inorg. Chem.* **2005**, *44* (7), 2245−2254.

(59) Andres, H.; Bominaar, E. L.; Smith, J. M.; Eckert, N. A.; Holland, P. L.; Münck, E. Planar Three-Coordinate High-Spin Fe$^{\mathrm{II}}$ Complexes with Large Orbital Angular Momentum: Mössbauer, Electron Paramagnetic Resonance, and Electronic Structure Studies. *J. Am. Chem. Soc.* **2002**, *124* (12), 3012−3025.

(60) Grubba, R.; Kaniewska, K.; Ponikiewski, Ł.; Cristóvão, B.; Ferenc, W.; Dragulescu-Andrasi, A.; Krzystek, J.; Stoian, S. A.; Pikies, J. Synthetic, Structural, and Spectroscopic Characterization of a Novel Family of High-Spin Iron(II) [(β-Diketiminate)-(Phosphanylphosphido)] Complexes. *Inorg. Chem.* **2017**, *56* (18), 11030−11042.

https://doi.org/10.1021/acs.inorgchem.3c03236
Inorg. Chem. 2024, 63, 2370−2387